

## ABSTRACT

FROESE, BRIAN CHRISTOPHER. Recirculating Target Design and Optimization for  $^{18}\text{F}$  Radionuclide Production. (Under the direction of Dr. J.M. Doster).

Current production of  $^{18}\text{F}$  by means of the (p,n) reaction with  $^{18}\text{O}$  enriched water is dominated by batch style water targets. Heat deposition from the proton beam limits targets of practical size to a maximum heat input of approximately 3 kW. As an alternative target technology, a recirculating target system is being developed by Bruce Technologies Inc. This recirculating system utilizes a pump to drive the  $^{18}\text{O}$  enriched water through a series of heat exchangers to remove the heat deposited by the proton beam. Work has already been done to model and optimize several main components in this system including the heat exchangers, pump, and beam shape. This work will investigate the design of the target body geometry using Computational Fluid Dynamics (CFD) methods to predict temperature and flow distributions within the target. Four designs were evaluated in this study. A prototype of the optimum design was then constructed and experimentally tested to compare the experimental pressure drop against predictions from CFD models. It was predicted that this recirculating target design can accommodate 6 kW of heat before the window temperature inside the target reaches saturation and over 15 kW before any part of the bulk fluid reaches the saturation temperature.

© Copyright 2013 Brian Froese

All Rights Reserved

Recirculating Target Design and Optimization for  $^{18}\text{F}$  Radionuclide Production

by  
Brian Christopher Froese

A thesis submitted to the Graduate Faculty of  
North Carolina State University  
in partial fulfillment of the  
requirements for the Degree of  
Master of Science

Nuclear Engineering

Raleigh, North Carolina

2013

APPROVED BY:

---

Dr. J. M. Doster  
Co-Chair of Advisory Committee

---

Dr. M. Stokely  
Co-Chair of Advisory Committee

---

Dr. W. Henderson

---

Dr. I. Bolotnov

## Biography

Brian Christopher Froese was born on December 26, 1988 to Mary Lee and Glenn Froese. He was raised in Pleasant Valley, New York and graduated from Arlington High School in 2007. After which he attended Syracuse University until May 2011, where he graduated Magna Cum Laude and with honors with a degree in Chemical Engineering. From several internships and projects in the nuclear field, he decided to pursue a graduate degree in Nuclear Engineering at North Carolina State University. After graduation he is starting work at Enercon Services, Inc.

## Acknowledgements

First I would like to thank all members of my graduate committee. I would especially like to thank Dr. J. M. Doster for all of his guidance and support as well as Dr. M. Stokely for leading me through the progression of target designs, setting up a suitable lab, and helping to formulate new ideas to pursue. I would also like to pay special thanks to Dr. B. Wieland for his continued enthusiasm and interest in my work. Further thanks go to Dr. I. Bolotnov for his expertise in CFD as well as to Michael Poorman for his expertise in metalwork design and using SolidWorks. This project would not have been possible without help from all parties mentioned.

# Table of Contents

List of Figures .....	vii
List of Tables .....	ix
List of Symbols and Abbreviations.....	x
Chapter 1 - Introduction.....	1
1.1. Background .....	1
1.2. Purpose .....	2
1.3. Related Work.....	5
Chapter 2 - System and Modeling Overview.....	7
2.1. Turbine Pump.....	7
2.2. Heat Exchangers.....	8
2.3. Calculating system flow rate .....	11
2.3.1. MTH ST21 Pump Curve.....	11
2.3.2. Heat Exchanger Pressure Drop .....	12
2.3.3. Elbow Pressure Drop .....	12
2.3.4. Tubing Pressure Drop .....	12
2.3.5. System Flow Rate .....	13
2.4. Target Inlet Temperature.....	13
2.5. Target Model Development .....	17
2.5.1. Beam Modeling.....	17
2.6. CFD Modeling using ANSYS CFX.....	20
2.6.1. CFD Overview .....	21
2.6.2. Turbulence Model.....	22
2.6.3. Boundary Conditions .....	24
2.6.4. Tetrahedron Elements .....	27
2.6.5. Boundary Layer Development.....	28
2.6.6. Proton Beam Heat Implementation.....	30
Chapter 3 - Target Designs and Analysis .....	33
3.1. Design Considerations.....	33
3.2. Recirculating Target 1 (RT-1).....	34
3.2.1. Design .....	34

3.2.2.	ANSYS Target Model: RT-1 .....	35
3.2.3.	RT-1 Pressure Drop and Inlet Temperature.....	37
3.2.4.	RT-1 Heated Model .....	39
3.2.5.	RT-1 Observations and Analysis .....	39
3.3.	RT-2 .....	40
3.3.1.	Design .....	40
3.3.2.	ANSYS Target Model: RT-2.....	41
3.3.3.	RT-2 Pressure Drop and Inlet Temperature.....	44
3.3.4.	RT-2 Heated Model .....	45
3.3.5.	RT-2 Observations and Analysis .....	45
3.4.	RT-3 .....	46
3.4.1.	Design .....	46
3.4.2.	ANSYS Target Model: RT-3.....	47
3.4.3.	RT-3 Pressure Drop and Inlet Temperature.....	49
3.4.4.	RT-3 Heated Model .....	50
3.4.5.	RT-3 Observations and Analysis .....	51
3.5.	RT-4 .....	52
3.5.1.	Design .....	52
3.5.2.	ANSYS Target Model: RT-4.....	53
3.5.3.	RT-4 Pressure Drop and Inlet Temperature.....	55
3.5.4.	RT-4 Heated Model .....	57
3.5.5.	RT-4 Observations and Analysis .....	57
3.5.6.	Verification through Fluent.....	58
3.5.7.	Experimental Verification.....	59
3.6.	Target Comparison.....	61
3.7.	Maximize Heat Input.....	62
3.7.1.	Critical Heat Flux Estimation .....	64
Chapter 4 -	Conclusions.....	66
4.1	Future Work .....	67
Bibliography	.....	69
Appendices	.....	71
Appendix A	.....	72

Sample System Volumetric Flow Rate MATLAB Code.....	72
Sample System Stream Temperatures MATLAB Code .....	73
Sample Exergy Heat Exchanger Calculator Output Data .....	74
Appendix B .....	75
Gaussian Standard Deviation and Plot Code .....	75
Appendix C .....	76
Sample MCNPX Input Deck .....	76
Sample MCNPX Heat Generation Output Tally .....	77
Appendix D.....	78
Sample Convergence Plots .....	78
Appendix E .....	81
Critical Heat Flux Calculation Code.....	81



## List of Figures

Figure 1: System overview .....	2
Figure 2: Specific ionization of alpha particles in air [23] .....	4
Figure 3: MTH ST21 pump [10].....	7
Figure 4: MTH ST21 pump performance curve; purple line was used [10].....	8
Figure 5: Exergy Series 10 Model 00268, lengths 4, 8 and 12 in. ....	9
Figure 6: MTH ST21 pump performance curve replicated in Excel .....	11
Figure 7: System diagram with five unknown temperatures .....	14
Figure 8: Process flowchart for calculating UA1, UA2 and target inlet temperature.....	16
Figure 9: Gaussian distribution for 10mm diameter beam, 85% transmission.....	19
Figure 10: Energy deposition mesh 14 MeV protons (left) and 27 MeV protons (right).....	20
Figure 11: Subdivisions of the near-wall region [4] .....	26
Figure 12: Undeveloped boundary layer (left) and developed boundary layer using Inflation (right) .....	29
Figure 13: Velocity distribution through pipe without boundary layer (left) and with boundary layer (right) .....	30
Figure 14: MCNPX heat generation distribution (left) vs. ANSYS CFX heat generation distribution (right).....	31
Figure 15: Heat generation rate through the center of the distributions shown in Figure 14 .	32
Figure 16: RT-1 assembled target [1] .....	34
Figure 17: Drawing of RT-1 [1].....	35
Figure 18: RT-1 extracted fluid, overhead view .....	36
Figure 19: RT-1 Mesh.....	36
Figure 20: RT-1 velocity streamlines, flow rate: 0.1 lb/s .....	36
Figure 21: RT-1 velocity distribution through cross-section of target chamber, flow rate: 0.1 lb/s.....	37
Figure 22: RT-1 pressure drop curve .....	38
Figure 23: RT-1 temperature distribution through a cross-section of the target chamber .....	39
Figure 24: RT-1 stagnation point location .....	40
Figure 25: RT-2.....	41
Figure 26: RT-2 extracted fluid .....	42
Figure 27: RT-2 mesh, overhead view.....	42
Figure 28: RT-2 velocity streamlines, flow rate: 0.1 lb/s .....	43
Figure 29: RT-2 velocity distribution through cross-section of target chamber, flow rate: 0.1 lb/s.....	43
Figure 30: RT-2 pressure drop curve .....	44
Figure 31: RT-2 temperature distribution through a cross-section of the target chamber .....	45
Figure 32: RT-3.....	47
Figure 33: RT-3 extracted fluid .....	47
Figure 34: RT-3 mesh .....	48
Figure 35: RT-3 velocity streamlines, flow rate 0.1 lb/s .....	48
Figure 36: RT-3 velocity distribution through cross-section of target, flow rate: 0.1 lb/s .....	48

Figure 37: RT-3 pressure drop curve .....	50
Figure 38: RT-3 temperature distribution .....	51
Figure 39: RT-3 velocity streamlines on top of the temperature distribution using 27 MeV protons.....	52
Figure 40: RT-4.....	53
Figure 41: RT-4 extracted fluid .....	54
Figure 42: RT-4 mesh .....	54
Figure 43: RT-4 velocity streamlines .....	54
Figure 44: RT-4 velocity distribution .....	55
Figure 45: RT-4 pressure drop curve .....	56
Figure 46: RT-4 temperature distribution .....	57
Figure 47: RT-4 window hotspot temperature distribution close-up.....	57
Figure 48: RT-4 velocity streamlines using Fluent.....	58
Figure 49: RT-4 velocity distribution through target cross-section using Fluent.....	59
Figure 50: Pressure drop experimental setup (top) and close-up of printed target (bottom)..	60
Figure 51: Experimental pressure drop vs. ANSYS predicted data.....	61
Figure 52: RT-4 temperature as a function of heat input.....	63

## List of Tables

Table 1: Heat exchanger maximum operating conditions .....	9
Table 2: Exergy 10 Series Model 00268 heat transfer capabilities .....	10
Table 3: Standard deviation for a given beam diameter and % enclosure.....	18
Table 4: 14 MeV vs. 27 MeV protons parameters.....	20
Table 5: RT-1 pressure drop and corresponding system flow rate .....	38
Table 6: RT-2 pressure drop and corresponding system flow rate .....	44
Table 7: RT-3 pressure drop and corresponding system flow rate .....	49
Table 8: RT-4 pressure drop and corresponding system flow rate .....	56
Table 9: Contending geometry design results.....	62
Table 10: RT-4 maximum temperatures .....	63

## List of Symbols and Abbreviations

A – Heat exchanger area, ft<sup>2</sup>

A<sub>x</sub> – Cross sectional area, ft<sup>2</sup>

a<sub>1</sub> – 0.31

C<sub>1</sub> – 0.1337 ft<sup>3</sup>/gallon

C<sub>ε1</sub> – 1.44

C<sub>ε2</sub> – 1.92

C<sub>μ</sub> – 0.09

D – Tubing diameter, ft

d – Diameter, ft

F – Gaussian distribution function in polar coordinates

F<sub>2</sub> – Blending function

f – Friction factor

f<sub>x</sub> – Full width half max in the x-direction, cm

f<sub>y</sub> – Full width half max in the y-direction, cm

G – Mass flux, lbm/s·ft<sup>2</sup>

h – Specific static enthalpy

h<sub>fg</sub> – Enthalpy of vaporization, BTU/lbm

h<sub>tot</sub> – Specific total enthalpy

I – Transmission factor

K – Loss coefficient

k – Turbulent kinetic energy

K<sub>HP</sub> – Subcooled multiplication factor

L –length, ft

$\dot{m}_c$  – Mass flow rate of coolant fluid, lbm/hr

$\dot{m}_h$  – Mass flow rate of heated target fluid, lbm/hr

$m_v$  – Volumetric flow rate, GPM

P<sub>k</sub> – Production rate of turbulence due to viscous forces

P<sub>kb</sub> – Represent buoyancy forces

$Pr_t$  – Turbulent Prandtl number  
 $P_{\epsilon_b}$  – Represent buoyancy forces  
 $P_{\omega_b}$  – Represent buoyancy forces  
 $p$  – Pressure, psi  
 $Q_{CHF,sat}$  – Critical heat flux under saturation conditions,  $W/cm^2$   
 $Q_{CHF,sub}$  – Critical heat flux under subcooled conditions,  $W/cm^2$   
 $Q_{HE}$  – Heat removed by a heat exchanger, Btu/hr  
 $Q_{tot}$  – Total heat input to system, Btu/hr  
 $r$  – Radius, mm  
 $Re$  – Reynolds Number  
 $S$  – Invariant measurement of shear strain  
 $S_E$  – Energy source  
 $S_m$  – Momentum source  
 $T$  – Temperature,  $^{\circ}F$   
 $T_1$  – Temperature of stream 1,  $^{\circ}F$   
 $T_2$  – Temperature of stream 2,  $^{\circ}F$   
 $T_3$  – Temperature of stream 3,  $^{\circ}F$   
 $T_{c1}$  – Temperature of coolant stream 1,  $^{\circ}F$   
 $T_{c2}$  – Temperature of coolant stream 2,  $^{\circ}F$   
 $T_{cold,i}$  – Temperature of cold stream inlet,  $^{\circ}F$   
 $T_{cold,o}$  – Temperature of cold stream outlet,  $^{\circ}F$   
 $T_{hot,i}$  – Temperature of hot stream inlet,  $^{\circ}F$   
 $T_{hot,o}$  – Temperature of hot stream outlet,  $^{\circ}F$   
 $t$  – Time  
 $U$  – Vector of the velocity  $U_{x,y,z}$   
 $U$  – Overall heat transfer coefficient,  $Btu/hr \cdot ft^2 \cdot ^{\circ}F$   
 $\bar{U}$  – Averaged velocity component  
 $u$  – Time-varying velocity component  
 $u^*$  – Friction velocity, ft/s

$v$  – Fluid velocity, ft/s

$y$  – Distance from the wall to the first node, ft

$y^+$  – Dimensionless number which expresses the distance from the wall to the first node

### *Greek Letters*

$\alpha$  – 5/9

$\beta$  – 0.075

$\beta'$  – 0.09

$\Delta h_{\text{sub}}$  – Inlet subcooling, BTU/lbm

$\Delta P_{\text{pump}}$  – Pressure rise across pump, psi

$\Delta P_{\text{HE1}}$  – Pressure drop through Exergy Model 10 Series 00286-02 heat exchanger, psi

$\Delta P_{\text{HE2}}$  – Pressure drop through Exergy Model 10 Series 00286-01 heat exchanger, psi

$\Delta P_{\text{elbow}}$  – Pressure drop through 90° elbow, psi

$\Delta P_{\text{target}}$  – Pressure drop through a specified target, psi

$\Delta T_{\text{m}}$  – Log Mean Temperature Difference, °F

$\Delta T_{\text{a}}$  – Specified temperature difference, °F

$\Delta T_{\text{b}}$  – Specified temperature difference, °F

$\delta$  – Identity matrix

$\varepsilon$  – Turbulent eddy dissipation

$\theta$  – Angle, radians

$\lambda$  – Thermal conductivity

$\mu$  – dynamic viscosity, lbm/hr·F

$\mu_{\text{eff}}$  – Effective dynamic viscosity

$\mu_{\text{t}}$  – turbulent dynamic viscosity

$\nu$  – Kinematic viscosity, ft<sup>2</sup>/s

$\nu_{\text{T}}$  – Turbulent kinematic viscosity

$\rho$  – Density, lbm/ft<sup>3</sup>

$\rho_{\text{v}}$  – Vapor density, lbm/ft<sup>3</sup>

$\rho_{\text{f}}$  – Fluid density, lbm/ft<sup>3</sup>

$\sigma$  – Surface Tension, lb/ft

$\sigma_k$  – 1.0

$\sigma_X$  – Standard deviation in the x-direction, cm

$\sigma_Y$  – Standard deviation in the y-direction, cm

$\sigma_\varepsilon$  – 1.3

$\sigma_\omega$  – 2

$\tau$  – Stress tensor

$\tau_w$  – Wall shear stress

$\omega$  – Turbulent frequency

# Chapter 1 - Introduction

## 1.1. Background

Positron emission tomography (PET) is a medical imaging modality for *in vivo* characterization of biomolecular processes. PET imaging is employed primarily for the diagnosis and staging of cancer and research is ongoing to make this technology more cost-effective as well as to increase production capabilities. This technique detects areas of high metabolic activity within the body which allows for abnormalities such as cancer to be identified.

PET imaging primarily utilizes the positron emitting radionuclide  $^{18}\text{F}$  which has a half-life of approximately 110 minutes, although other positron-emitting radionuclides such as  $^{15}\text{O}$ ,  $^{13}\text{N}$ , or  $^{11}\text{C}$  can also be used.  $^{18}\text{F}$  is typically used to synthesize [ $^{18}\text{F}$ ]fluorodeoxyglucose (FDG), a glucose analog [5]. FDG is particularly useful for detecting cancer because cancer cells are known to grow at an accelerated rate and thereby take in sugars faster than other cells in the body. This leads to an increased concentration of FDG in cancer cells which makes for easier detection.

$^{18}\text{F}$  is traditionally produced through the (p,n) reaction with  $^{18}\text{O}$  enriched water [2]. Heat is produced from the collision of these protons with either the  $^{18}\text{O}$  enriched water or the target device itself. The decay of  $^{18}\text{F}$  occurs by  $\beta^+$  emission 97% of the time and electron capture 3% of the time. The positron quickly annihilates with an electron (within a few millimeters), producing two 511 keV annihilation photons that travel in opposite directions.



The basis of PET imaging is that scintillators can be used to detect these 511 keV photons in coincidence. The time at which each 511 keV photon is detected can be correlated to the original position at which the decay occurred, creating a 3D map. As positrons can travel a few millimeters, this limits the spatial resolution of PET [5].

## 1.2. Purpose

The purpose of this research is to optimize the design of a recirculating water target for the production of  $^{18}\text{F}$ . The design goal is for these targets to have heat rejection capabilities in excess of 10 kW. Current  $^{18}\text{F}$  production is batch-based and limited to approximately 3 kW before the size required becomes cost-ineffective. A recirculating system pumps target water through a series of heat exchangers allowing for more effective heat transfer.

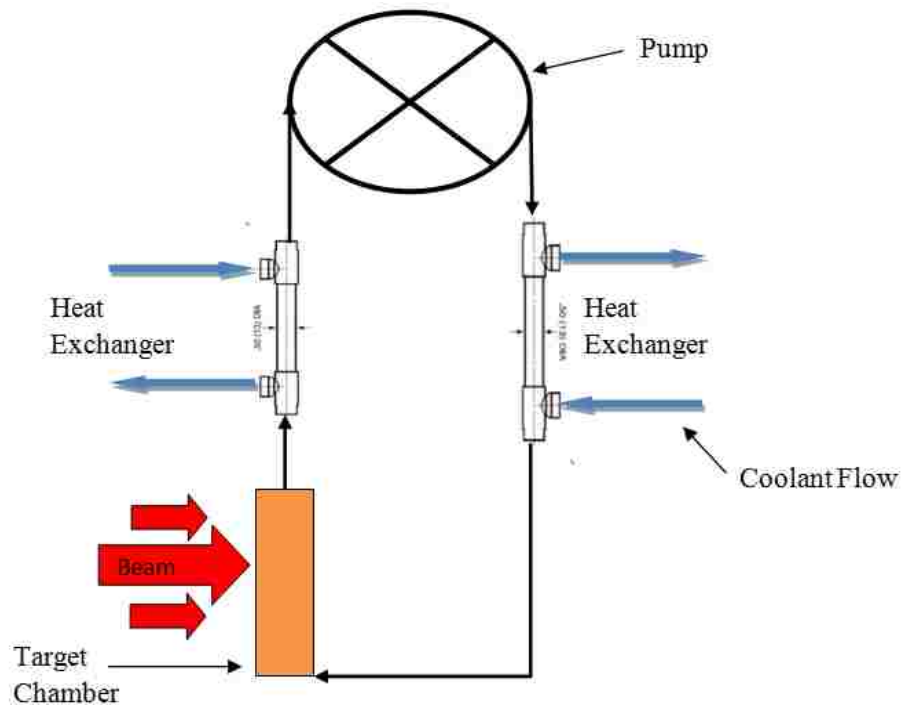


Figure 1: System overview

A basic overview of the system is shown in Figure 1. Target water passes through the target chamber where it is struck by the proton beam, producing heat. The target water then enters a heat exchanger, is pumped through a second heat exchanger and returned to the target. Specific aims of this research are to:

- Develop Computational Fluid Dynamics (CFD) models of candidate target geometries. The CFD package utilized in this work is ANSYS CFX.
- Design, simulate, and optimize candidate target geometries for a given heat input.
- Construct a prototype of the most promising design and compare the experimentally determined pressure drop against model predictions.
- Predict the maximum production yield for the selected design.

There are a variety of factors which need to be considered when designing a target. A constraint imposed on the target design in this work, was that no location within the target could exceed the fluid saturation temperature, leading to the potential for having subcooled boiling. This was chosen because ANSYS CFX is not capable of modeling boiling. The maximum temperatures within the target typically occur in two locations. The most common hotspot is at the window-fluid interface in the center of the beam-strike. The window is typically made of a 0.001'' thick piece of Havar. This high strength metal alloy has a density of  $8.3 \text{ g/cm}^3$ , significantly higher than that of the target water (approximately  $1 \text{ g/cm}^3$ ). The number of particle collisions is a strong function of the density of the material and therefore, the window exhibits the highest volumetric heat generation rate in the system.

The other hotspot is located at the Bragg peak, the position of which is dictated by the proton energy. As protons move through a medium and slow down, it becomes increasingly

probable that they will capture an electron [23]. Once this occurs, the specific ionization abruptly drops to zero. This leads to what is referred to as the Bragg peak, which is the position where most of the protons interact with an electron and consequently a location of high heat generation. This is shown in Figure 2 for the case of alpha particles in air.

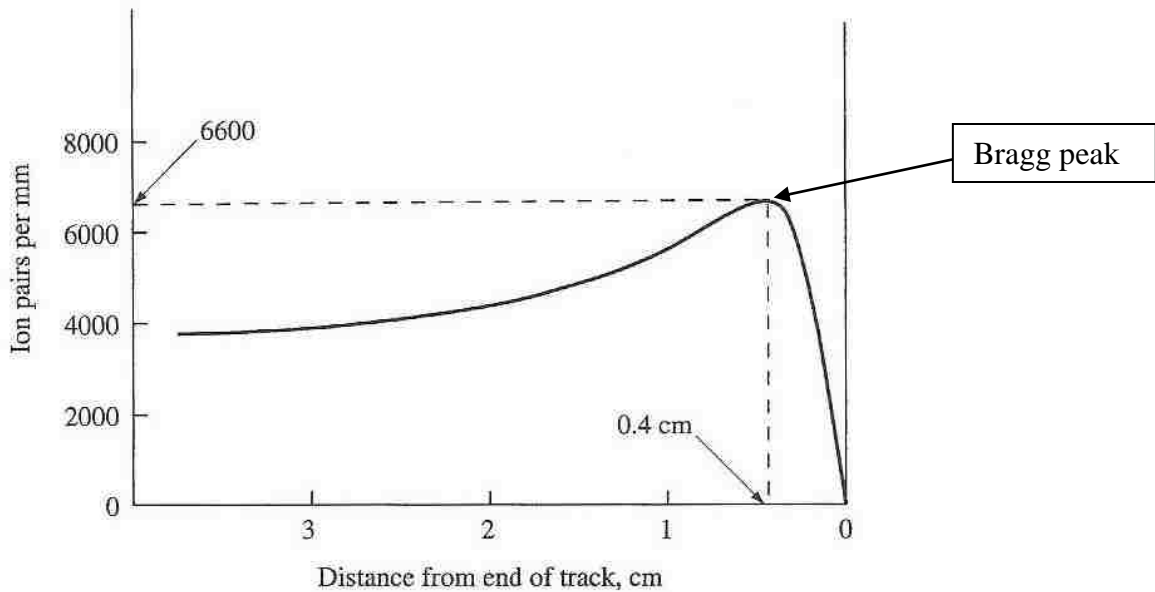


Figure 2: Specific ionization of alpha particles in air [23]

The highest proton energy attainable from the CS-30 cyclotron at the Duke University PET facility is 27 MeV, which was chosen as the upper limit for this study. This facility has supported prior target work with Bruce Technologies inc. and representative of other cyclotrons being used in the industry. The benefit of using higher proton energy is less energy is deposited in the window. The maximum  $\frac{mCi}{kW}$  for  $^{18}\text{F}$  production occurs at a proton energy of 14 MeV, which set the lower limit of this study [15]. Proton energies between 14 and 27 MeV were also considered, however these two produced the best results in terms of yield versus energy input.

System volume is an additional design consideration. Due to the high cost of enriched  $^{18}\text{O}$ , a design objective is to keep the system volume to a minimum. However, smaller target volumes typically result in higher pressure drops, increasing the pumping requirements.

Four main target configurations were considered, with each undergoing several iterations of design changes. The final (optimum) design of each is presented here.

### 1.3. Related Work

Bruce Technologies Inc. in collaboration with North Carolina State University has been investigating recirculating style targets for upwards of ten years. In May, 2003 Bruce Technologies Inc. patented a recirculating target and method for producing radionuclide [27]. Significant progress has been made on the pump design, beam modeling, heat exchanger selection, and integrated system layout.

The idea of a recirculating target was first introduced in 1977 by Oak Ridge National Laboratory in coordination with Massachusetts Institute of Technology. A system layout similar to the one proposed in this research was employed in which target fluid flows through the target chamber, into a heat exchanger, is pumped through a second heat exchanger and then returns to the target. The original design was for a 22 MeV, 250  $\mu\text{A}$  beam and called for a total system volume of 240 ml. A catalytic recombination unit was needed in order to recover the large amount of  $\text{H}_2$  and  $^{18}\text{O}_2$  gases produced as a consequence of the high system volume [6].

Ion Beam Applications (IBA), a company founded in 1986, manufactures nearly all equipment needed for  $^{18}\text{F}$  production including but not limited to: cyclotrons, batch-style targets, and chemistry systems to produce FDG [8]. Their most recent target called the Nirta<sup>®</sup>

$^{18}\text{F}$  Fluoride is a batch-style target capable of producing up to 13 curies per run. In May, 2003 IBA patented a recirculating target design [9]. The design assumes a 16 MeV, 40  $\mu\text{A}$  proton beam. Flow can be diverted out of the main loop to extract the  $^{18}\text{F}$ , after which the remaining enriched water can be fed back into the system. Additional  $^{18}\text{O}$  enriched water can be added through a feed line during operation in order to replenish target fluid which was either lost to leakage or  $^{18}\text{F}$  production.

## Chapter 2 - System and Modeling Overview

In this section we review the current status of the recirculating target system, and present the computational methods used for the target body design.

### 2.1. Turbine Pump

Pump performance is a crucial part of the recirculating target system. Several design considerations which need to be taken into account when selecting a pump are:

- Maximum flow rate
- Small system volume
- Little to no leakage rate
- Large pressure head

The ST21 Series DC Brushless Regenerative Turbine Pump by MTH is proposed for the target system because it meets all of these requirements [10]. The MTH website provides the performance curve for this pump shown in Figure 4.

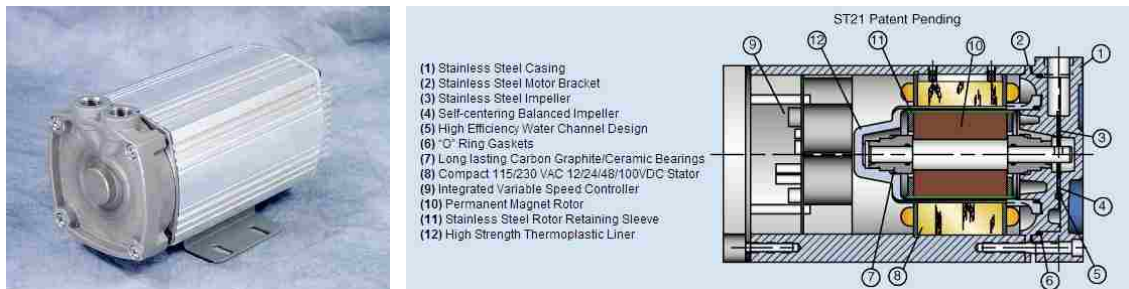


Figure 3: MTH ST21 pump [10]

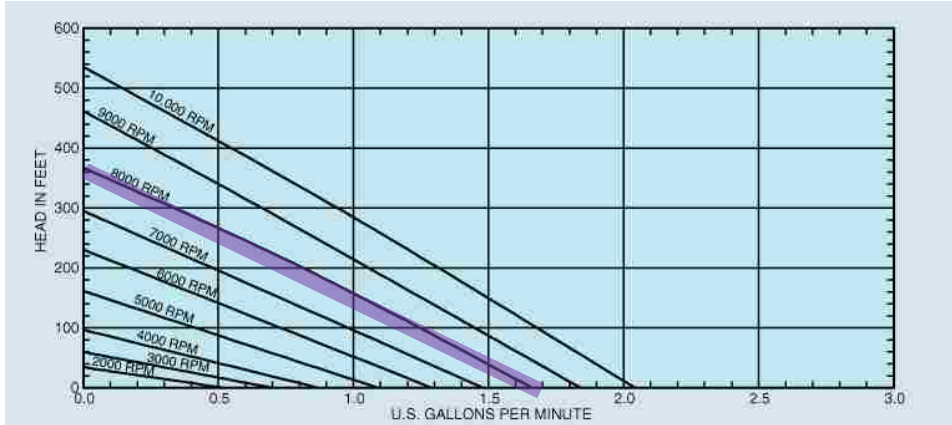


Figure 4: MTH ST21 pump performance curve; purple line was used [10]

It is expected the pump will run at 8000 RPM, which yields a good balance between high flow rates and reasonably long seal life [24]. Given this pump speed, flow rates of over 1.6 GPM are achievable. Another important attribute of this pump is its ability to handle volatile fluid. According to the MTH website, the pump can handle vapor volume fractions of up to 20%, minimizing the possibility of vapor lock [10]. This is desirable in the event that boiling occurs unexpectedly in the target.

Testing is still underway to determine the effects of radiation damage as well as the possibility and repercussions of a seal failure. This poses a risk if the highly radioactive target fluid leaks out of the system. In the event that this pump cannot be used due to seal failures, a custom built pump which prevents leakage may be purchased instead, however custom pumps such as this are fairly expensive.

## 2.2. Heat Exchangers

Heat exchangers for this system have already been selected and tested [2]. The Exergy 10 Series Model 00268 was chosen for its low volume and high heat rejection capabilities

[12]. This model comes in three different lengths: 4, 8 and 12 in. long. Table 1 shows the maximum operating conditions associated with these heat exchangers. The internal shell diameter of all three types is 0.50 in.

Table 1: Heat exchanger maximum operating conditions

Tube-side pressure (psi)	1500
Shell-side pressure (psi)	1000
Temperature (°F)	800
Fluid Temperature Difference (°F)	125

The maximum pressure and temperature constraints are well within the limits of this project; however the maximum fluid temperature difference does impose a constraint on the system design. Exergy uses a Nickel-Chromium brazing to connect the primary side tubes to the inlet and outlet heads. Although this increases the reliability of the heat exchanger, it is more susceptible to thermal cracking at high temperature differences [2].



Figure 5: Exergy Series 10 Model 00268, lengths 4, 8 and 12 in.



Exergy uses the Maximum Average Temperature Difference (MATD) to set their temperature difference constraint of 125 °F.

$$MATD = \left( \frac{T_{hot,i} + T_{hot,o}}{2} \right) - \left( \frac{T_{cold,i} + T_{cold,o}}{2} \right) \quad (1)$$

The Exergy website provides a calculator which predicts the heat transfer rate for a particular model given the tube and shell side inlet temperatures and flow rates. Table 2 gives predicted heat exchanger performance for inlet conditions similar to what is expected to be seen with the recirculating targets.

Table 2: Exergy 10 Series Model 00268 heat transfer capabilities

Model	Tube Length (in.)	Tube Volume (ml)	Tube-side Flow Rate (GPM)	Shell- Side Flow Rate (GPM)	T <sub>hot,i</sub> (°F)	T <sub>cold,I</sub> (°F)	Heat Transfer (W)
00268-02	4.00	2.01	1.00	3.00	150	60	2148
00268-01	8.00	4.00	1.00	3.00	150	60	3802
00268-03	12.00	6.00	1.00	3.00	150	60	5126

As shown earlier in Figure 1, the integrated system is expected to have one Series 10 Model 00268-02 heat exchanger (4 in. long) immediately after the target, followed by one Series-10 Model 00268-01 heat exchanger (8 in. long) immediately after the pump. This will provide sufficient heat removal for the beam currents and energies anticipated during deployment, while keeping the maximum average temperature difference within the MATD constraint.

## 2.3. Calculating system flow rate

The system-wide flow rate for a target geometry design affects the maximum temperature predicted inside the target as well as the heat exchanger performance. A code was written to calculate the system flow rate given the pump performance curve and pressure drop curves for the two heat exchangers, piping, and target. The pressure drop curves for the target were calculated in ANSYS CFX for each candidate design and are given in Chapter 3.

### 2.3.1. MTH ST21 Pump Curve

From the pump performance curve given in Figure 4, a best fit linear trendline was created for the ST21 Series DC Brushless Regenerative Turbine Pump operating at 8000 RPM.

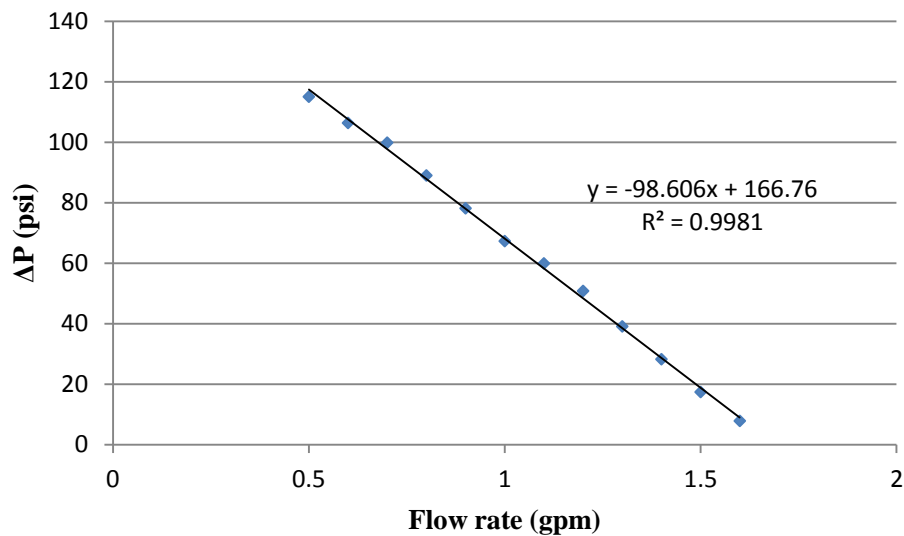


Figure 6: MTH ST21 pump performance curve replicated in Excel

From Figure 6, the pressure rise across the pump can be expressed as a function of volumetric flow rate in GPM as:

$$\Delta P_{pump}(m_v) = -98.606 * (m_v) + 166.76 \quad (2)$$

### 2.3.2. Heat Exchanger Pressure Drop

Heat exchanger pressure drop curves were available from prior work [2]. For the Series 10 Model 00268-02 heat exchanger, the pressure drop can be expressed as a polynomial:

$$\Delta P_{HE1}(m_v) = 4.4379 * (m_v)^2 - 0.7200 * (m_v) + 1.374 \quad (2)$$

Similarly, for the Model 00268-01 heat exchanger, the pressure drop can be expressed as:

$$\Delta P_{HE2}(m_v) = 4.0963 * (m_v)^2 - 1.398 * (m_v) - 0.7037 \quad (3)$$

### 2.3.3. Elbow Pressure Drop

From the system overview shown in Figure1, the piping network contains one 90 degree elbow. The pressure drop across this bend is calculated using the following equation:

$$Head = K \left( \frac{v^2}{2g} \right) \quad (4)$$

where  $K=0.5$  for  $90^\circ$  elbows [19]. Converting the pressure drop to psi and replacing velocity with volumetric flow rate (GPM), gives the pressure drop across a  $1/8^{\text{th}}$  inch diameter elbow as:

$$\Delta P_{elbow}(m_v) = 2.31 * m_v^2 \quad (5)$$

### 2.3.4. Tubing Pressure Drop

It was assumed that 6 inches of  $1/8^{\text{th}}$  inch tubing would be sufficient to connect all components of the system. The pressure drop due to tubing is given by the following equations:

$$\Delta P_{tubing} (m_v) = \frac{fL}{D} * \frac{\rho(\frac{C_1 m_v}{A_x})^2}{2} \quad (6)$$

$$f = 0.184Re^{-0.2} \quad (7)$$

$$Re = \frac{\rho v D}{\mu} \quad (8)$$

The friction factor formula is for fully developed turbulent flow over smooth surfaces with  $Re > 2 \times 10^4$  [20]. In this study, the Reynolds number through the tubing is greater than  $6 \times 10^4$ .

### 2.3.5. System Flow Rate

Utilizing Equations 2-8, the system volumetric flow rate  $m_v$  can be calculated for each target geometry by solving the equation:

$$\Delta P_{pump} (m_v) = \Delta P_{HE1} (m_v) + \Delta P_{HE2} (m_v) + \Delta P_{tubing} (m_v) + \Delta P_{elbow} (m_v) + \Delta P_{target} (m_v) \quad (9)$$

A code was written to solve this in MATLAB. A sample for one of the targets is attached in Appendix A. Total system flow rates for the contending target designs are included in Chapter 3.

## 2.4. Target Inlet Temperature

Target inlet temperature is directly related to the maximum temperature inside the target and is a required inlet condition when setting up a target model in ANSYS CFX. The target inlet temperature as a function of heat input was calculated for each target design given their unique system flow rate. This was done by writing energy balances around the target and each of the two heat exchangers. This results in 5 equations in terms of the 5 fluid stream temperatures illustrated in Figure 7. It was assumed that the system is perfectly insulated and that no heat is lost to the surroundings.

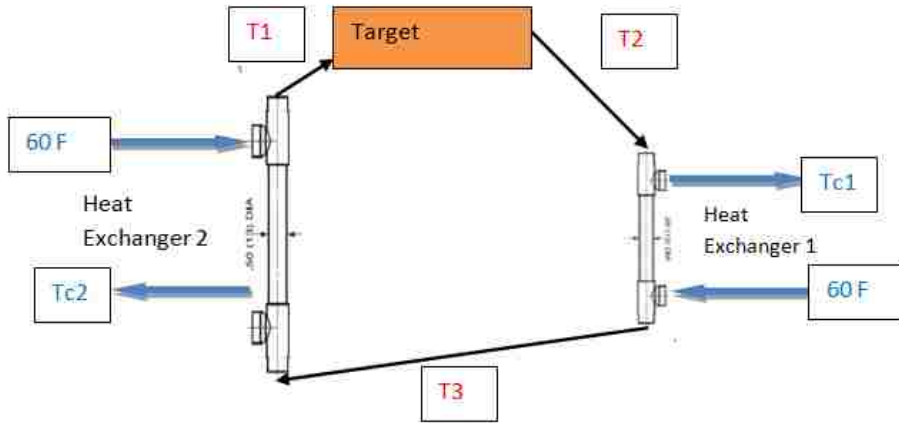


Figure 7: System diagram with five unknown temperatures

$$Q_{tot} = \dot{m}_h C_p (T_2 - T_1) \quad (10)$$

$$\dot{m}_h C_p (T_2 - T_3) = UA_1 \left( \frac{(T_3 - 60^{\circ}F) - (T_2 - T_{C1})}{\ln \left( \frac{T_3 - 60^{\circ}F}{T_2 - T_{C1}} \right)} \right) \quad (11)$$

$$\dot{m}_h C_p (T_2 - T_3) = \dot{m}_c C_p (T_{C1} - 60^{\circ}F) \quad (12)$$

$$\dot{m}_h C_p (T_3 - T_1) = UA_2 \left( \frac{(T_1 - 60^{\circ}F) - (T_3 - T_{C2})}{\ln \left( \frac{T_1 - 60^{\circ}F}{T_3 - T_{C2}} \right)} \right) \quad (13)$$

$$\dot{m}_h C_p (T_3 - T_1) = \dot{m}_c C_p (T_{C2} - 60^{\circ}F) \quad (14)$$

Solving for  $T_1$  yields the inlet temperature for the target. Equations 10-14 were solved using a code written in MATLAB. A copy of this code is also provided in Appendix A.

The overall heat transfer coefficients  $UA_1$  and  $UA_2$ , were calculated using the Exergy Online Heat Exchanger Calculator for each of the four system flow rates. By inputting the system flow rate, pressure, and inlet temperatures, the outlet temperatures and total heat

removed are calculated by the program. The value of UA can then be back-calculated by using the following equations:

$$Q_{HE} = UA\Delta T_m \quad (15)$$

$$\Delta T_m = \frac{\Delta T_b - \Delta T_a}{\ln\left(\frac{\Delta T_b}{\Delta T_a}\right)} \quad (16)$$

$$\Delta T_a = T_{hot,o} - T_{cold,i} \quad (17)$$

$$\Delta T_b = T_{hot,i} - T_{cold,o} \quad (18)$$

The problem is iterative as UA changes with the coolant inlet temperature. A flowchart for computing UA is shown in the following process diagram.

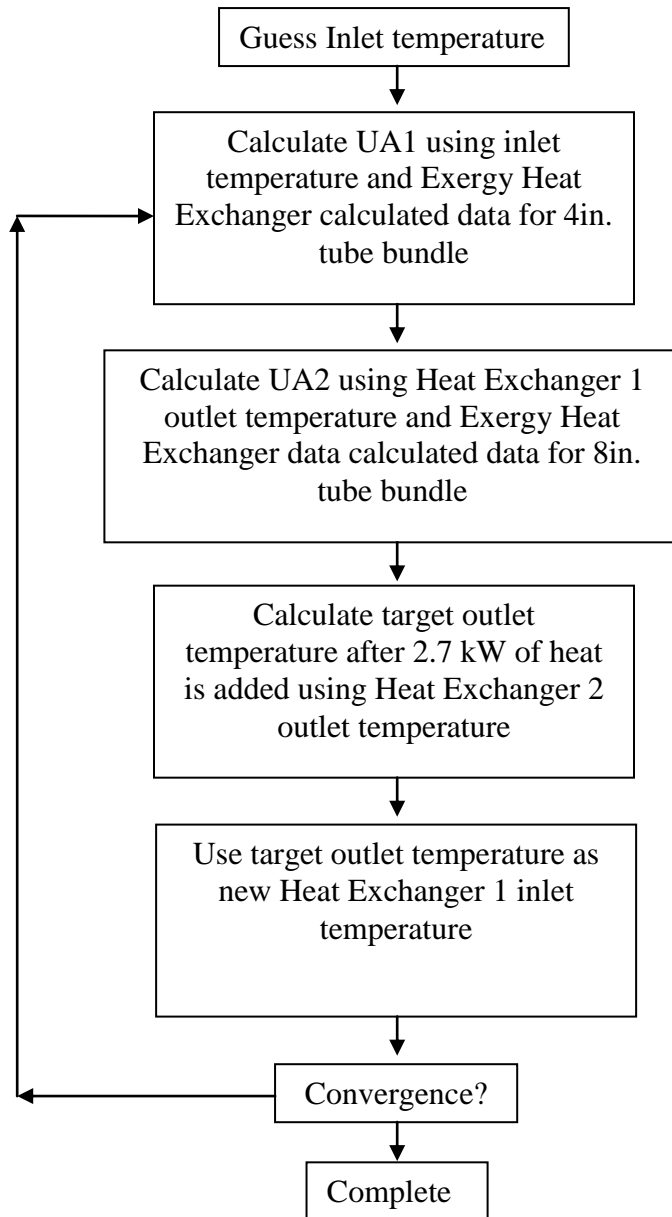


Figure 8: Process flowchart for calculating UA1, UA2 and target inlet temperature

## 2.5. Target Model Development

Targets were modeled in ANSYS CFX, a computational fluid dynamics program which utilizes the Finite Element Method (FEM) to solve the partial differential equations governing heat transfer and fluid flow. The primary purpose of these models is to predict the maximum temperature in the target fluid which serves as the limiting criteria for the target. Volumetric heat generation data was produced from MCNPX and imported into ANSYS CFX. This section will contain an overview of how these two programs were used in target modeling.

### 2.5.1. Beam Modeling

MCNPX is a general-purpose Monte Carlo radiation transport code for modeling the interaction of neutral and charged particles with matter. MCNPX was used to produce energy deposition tallies due to proton interactions in the target water and the Havar window. The output tally was reformatted as point-wise volumetric heat generation rates and imported directly into ANSYS CFX.

The beam is modeled as a Gaussian distribution, the width of which is dictated by the full width at half maximum (FWHM). Both the target fluid and Havar window were included in the model. A sample input deck and results file are shown in Appendix C. The number of particles was chosen to insure statistically meaningful results. This typically occurred at around one million particle histories; however a general idea of the distribution can be obtained by using as few as twenty thousand.



The beam was modeled such that 85% of the Gaussian was contained within the beam radius. MCNPX requires the FWHM as input. This can be calculated as [13]:

$$f_x = (8 \ln(2))^{\frac{1}{2}} \sigma_x \quad (19)$$

$$f_y = (8 \ln(2))^{\frac{1}{2}} \sigma_y \quad (20)$$

A code was written to calculate the standard deviation  $\sigma_x$  and  $\sigma_y$  given a desired transmission factor and beam diameter. The transmission factor is the fraction of the Gaussian distribution used. This is done by integrating the Gaussian distribution function over the beam area as indicated in equations 21 and 22 and incrementally increasing the standard deviation until the desired transmission factor is achieved.

$$F(r, \theta) = \frac{1}{2\pi\sigma_x\sigma_y} \cdot \exp\left(\frac{-r^2 \cos(\theta)^2}{2\sigma_x^2}\right) \cdot \exp\left(\frac{-r^2 \sin(\theta)^2}{2\sigma_y^2}\right) \quad (21)$$

$$I = \int_0^{2\pi} \int_0^r F(r, \theta) \cdot r dr d\theta \quad (22)$$

Table 3 gives the standard deviations for a given transmission factor and the range of diameters used in this study. The MATLAB code written to perform these calculations is included as Appendix B.

Table 3: Standard deviation for a given beam diameter and % enclosure

Diameter (mm)	$\sigma$ (mm) for 95%	$\sigma$ (mm) for 90%	$\sigma$ (mm) for 85%	$\sigma$ (mm) for 80%
10	2.038	2.327	2.565	2.785
9	1.834	2.094	2.308	2.507
8	1.630	1.862	2.052	2.228
7	1.427	1.629	1.796	1.950

Two and three dimensional representations of the beam distribution are shown in Figure 9.

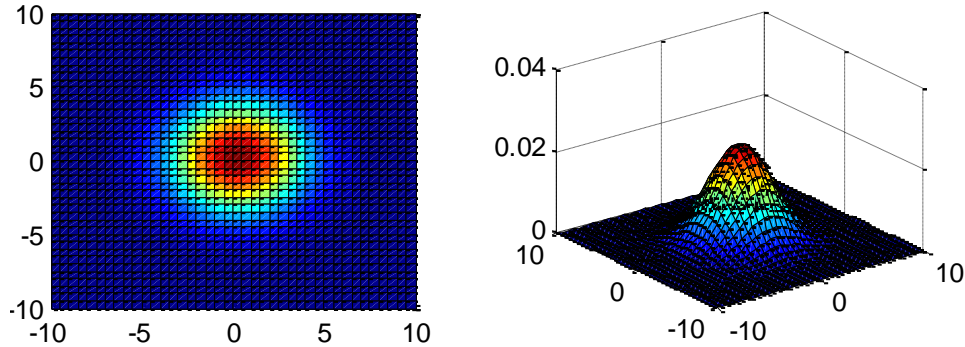


Figure 9: Gaussian distribution for 10mm diameter beam, 85% transmission

In this study, proton energies of 14 MeV and 27 MeV were considered. 14 MeV was chosen because it creates the largest amount of product per unit kW input while 27 MeV deposits the least amount of energy into the window.

Figure 10 shows a side-by-side comparison of the energy deposition rates produced by MCNPX for 14 MeV and 27 MeV protons through 1/1000'' Havar and water. The target is 10mm in diameter and 10mm deep. The figure is for a cross section through the center of the cylinder. The colors scale to the relative energy deposition, with red being the highest and blue being the lowest.

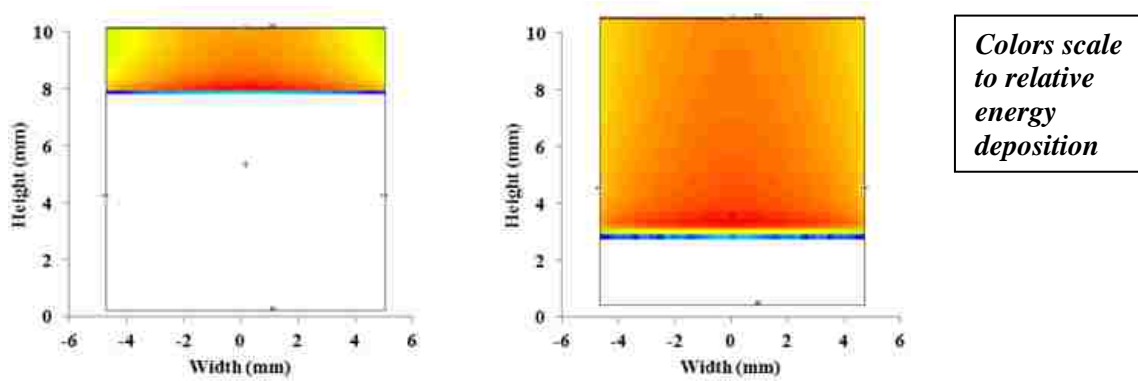


Figure 10: Energy deposition mesh 14 MeV protons (left) and 27 MeV protons (right)

Table 4: 14 MeV vs. 27 MeV protons parameters

Proton Energy:	Stopping Distance (mm)	Heat deposited in window	Heat Deposited in fluid
14 MeV	2.2	3.29%	96.71%
27 MeV	7.6	1.05%	98.95%

As shown in Table 4, more than three times the amount of heat is deposited in the Havar window when using 14 MeV as opposed to 27 MeV protons.

## 2.6. CFD Modeling using ANSYS CFX

ANSYS CFX was utilized for its ability to model fluid flow and heat transfer through complex fluid and solid geometries using FEM and serves as a low cost alternative to constructing and testing prototype components. The modeling process is split into four stages [3]:

1. Creating the Geometry/Mesh
2. Defining the Physics of the Model
3. Solving the CFD Problem
4. Visualizing the Results in the Post-Processor

The geometry can be created using the ANSYS DesignModeler or imported from a Computer Aided Design (CAD) program. For this study, geometries were created using SolidWorks 2012, a 3D CAD software package [11]. When creating a geometric representation of the design, it is important to encompass all aspects of the design which have a significant impact on the results. However, care must be taken not to overcomplicate the design as this may stall the ANSYS meshing program or the ANSYS solver. An example of such is screw holes. In many cases screw holes are not in the area of interest, however the number of elements which are needed to mesh such a feature is very large.

### 2.6.1. CFD Overview

Computational Fluid Dynamics (CFD) is a tool used to simulate the physical processes associated with heat transfer and fluid flow. This is done by solving the Navier-Stokes equations over a particular computational domain. The instantaneous equations for mass, momentum, and energy conservation are given as [18]:

$$\frac{\partial \rho}{\partial t} + \nabla \cdot (\rho U) = 0 \quad (23)$$

$$\frac{\partial(\rho U)}{\partial t} + \nabla \cdot (\rho U \otimes U) = -\nabla p' + \nabla \cdot \mu \left( \nabla U + (\nabla U)^T - \frac{2}{3} \delta \cdot U \right) + S_m \quad (24)$$

$$\frac{\partial(\rho h_{tot})}{\partial t} - \frac{\partial p}{\partial t} + \nabla \cdot (\rho U h_{tot}) = \nabla \cdot (\lambda \nabla T) + \nabla \cdot (U \tau) + U \cdot S_m + S_E \quad (25)$$

$$h_{tot} = h + \frac{1}{2} U^2 \quad (26)$$

Where  $\nabla \cdot (U \tau)$  represents the work due to viscous stresses and  $U \cdot S_m$  represents the work due to external momentum sources. These equations have no general analytic solution; however they can be discretized and solved numerically [4]. The solution procedure is iterative and ANSYS CFX calculates mass, momentum, energy, and turbulence residuals

until they reach a selected convergence value. The default relative residual value for each is 1e-4; however a value of 5e-5 is utilized in this study. Once this level of convergence is achieved there appeared to be no noticeable difference in the calculated values if additional iterations are done. Sample residual graphs are shown in Appendix D.

## 2.6.2. Turbulence Model

The Navier-Stokes equations in theory are able to solve both laminar and turbulent flow systems [18]. However, the length and time scales needed for Direct Numerical Simulation (DNS) of turbulent flow in the geometries of interest surpasses the computing capabilities currently available. Therefore in order to simulate turbulent flow, ANSYS CFX makes use of turbulence models. The majority of these models utilize modified Navier-Stokes equations in which the variables contain both an averaged and time-varying component. These are called the Reynolds Averaged Navier-Stokes (RANS) equations. An example of the velocity  $U$  is given as the following, Where  $\bar{U}$  is the average component and  $u$  is the time-varying component [18]:

$$U = \bar{U} + u \quad (27)$$

$$\bar{U} = \frac{1}{\Delta t} \int_t^{t+\Delta t} U dt \quad (28)$$

The turbulence models are reflected in the calculation of the time-varying component of the effective viscosity term,  $\mu_t$ . The new set of Navier-Stokes equations thus becomes:

$$\frac{\partial \rho}{\partial t} + \nabla \cdot (\rho U) = 0 \quad (29)$$

$$\frac{\partial(\rho U)}{\partial t} + \nabla \cdot (\rho U \otimes U) = -\nabla p' + \nabla \cdot (\mu_{\text{eff}}(\nabla U + (\nabla U)^T)) + S_m \quad (30)$$

$$\frac{\partial(\rho h_{\text{tot}})}{\partial t} - \frac{\partial p}{\partial t} + \nabla \cdot (\rho U h_{\text{tot}}) = \nabla \cdot (\lambda \nabla T + \frac{\mu_t}{Pr_t} \nabla h) + \nabla \cdot (U \cdot (\tau - \rho \overline{u \otimes u})) + S_E \quad (31)$$

$$\mu_{eff} = \mu + \mu_t \quad (32)$$

One of the most common turbulence models used throughout the industry is the k-ε model [25]. This model is robust and correcting functions have been developed to increase the accuracy at the wall. While the k-ε model offers a good combination of accuracy and robustness, there are several situations where this model fails [4].

- Flows with boundary layer separation
- Flows with sudden changes in the mean strain rate
- Flows with rotating fluids
- Flows over curved surfaces

In target design, there are two important geometrical considerations which influence the appropriate computational models. The first is minimizing the volume of the target. This will typically involve an expansion and contraction piece at the inlet and outlet. The second is to avoid sharp corners in order to prevent areas of stagnation. Both of these characteristics directly conflict with the k-ε model. The k-ω based Shear-Stress-Transport (SST) model is a turbulence model based on the k-ω model which gives highly accurate predictions for flow separations and therefore it was utilized in this research [26]. This model differs from the k-ε model in that it takes into account the transport of turbulent shear stress.

The k-ε model is given by the following differential equations:

$$\frac{\partial \rho k}{\partial t} + \nabla \cdot (\rho k U) = \nabla \cdot \left[ \left( \mu + \frac{\mu_t}{\sigma_k} \right) \nabla k \right] + P_k + P_{kb} - \rho \varepsilon \quad (33)$$

$$\frac{\partial \rho \varepsilon}{\partial t} + \nabla \cdot (\rho \varepsilon U) = \nabla \cdot \left[ \left( \mu + \frac{\mu_t}{\sigma_\varepsilon} \right) \nabla \varepsilon \right] + \frac{\varepsilon}{k} (C_{\varepsilon 1} (P_k + P_{\varepsilon b}) - C_{\varepsilon 2} \rho \varepsilon) \quad (34)$$

where  $C_{\varepsilon 1}$ ,  $C_{\varepsilon 2}$ ,  $\sigma_k$  and  $\sigma_\varepsilon$  are constants;  $P_{kb}$  and  $P_{\varepsilon b}$  represent the influence of the buoyancy forces and  $P_k$  is the turbulence production due to viscous forces. The k- $\varepsilon$  model is used to solve for the turbulent portion of the viscosity which is then used to calculate the effective viscosity  $\mu_{\text{eff}}$  in the Navier-Stokes Equation.

$$\mu_t = C_\mu \rho \frac{k^2}{\varepsilon} \quad (35)$$

The k- $\omega$  model on the other hand is given as:

$$\frac{\partial \rho k}{\partial t} + \nabla \cdot (\rho k \mathbf{U}) = \nabla \cdot \left[ \left( \mu + \frac{\mu_t}{\sigma_k} \right) \nabla k \right] + P_k + P_{kb} - \beta' \rho k \omega \quad (36)$$

$$\frac{\partial \rho \omega}{\partial t} + \nabla \cdot (\rho \omega \mathbf{U}) = \nabla \cdot \left[ \left( \mu + \frac{\mu_t}{\sigma_\omega} \right) \nabla \omega \right] + \alpha \frac{\omega}{k} P_k + P_{\omega b} - \beta \rho \omega^2 \quad (37)$$

$$\mu_t = \rho \frac{k}{\omega} \quad (38)$$

Where  $\beta$ ,  $\beta'$ ,  $\alpha$ ,  $\sigma_k$ , and  $\sigma_\omega$  are constants;  $P_{\omega b}$  represents an additional buoyancy term. The k- $\omega$  model fails to predict the onset of flow separation along smooth surfaces, ultimately because it does not account of turbulent shear stress [26]. To correct for this, the shear stress transport (SST) model implements a limiter on the eddy-viscosity as:

$$\nu_t = \frac{a_1 k}{\max(a_1 \omega, S F_2)} \quad (39)$$

$$\nu_t = \mu_t / \rho \quad (40)$$

where  $a_1$  is a constant and  $F_2$  is a blending function. This results in more accurate predictions of flow separation under large pressure gradients.

### 2.6.3. Boundary Conditions

In addition to specifying the inlet temperature and mass flow rate, the inlet was also given a zero gradient boundary condition, which means the velocity gradient perpendicular to

the boundary is zero [4]. This is commonly used for fully developed turbulence conditions and was used for all target models as the overall system flow rate is well into the turbulent regime. A study was done to ensure the piping between the heat exchanger and the target was sufficiently long to produce fully developed flow prior to entering the target and the heat exchanger did not affect the velocity profile entering the target.

A No-Slip Wall Condition was also employed where the fluid velocity at the wall is forced to zero and gradually becomes fully developed. To better illustrate how the wall is treated, Figure 11 shows the near wall velocity profile. This can be divided into three regions [4].

1. Turbulent Layer: This is the fully developed region away from the wall
2. Logarithmic Layer: Turbulence dominates the mixing process but effects are felt from the viscous forces
3. Viscous sublayer: Viscous forces dominate momentum and heat transfer. Flow is almost laminar-like



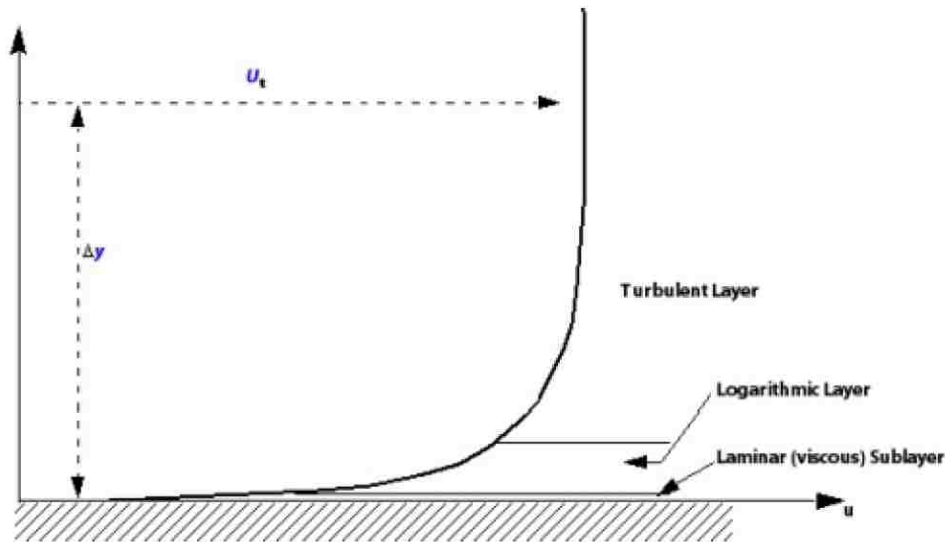


Figure 11: Subdivisions of the near-wall region [4]

Since analytical solutions to the Navier-Stokes equations are only available for simplistic flow geometries, ANSYS CFX utilizes wall functions to solve for variables at the boundary. This is advantageous because it requires less computational effort than fully discretizing the boundary. When ANSYS CFX solves a model, the solution to the boundary layers are obtained from solving the fluid conservation equations and called the ‘conservative values’. These conservative values do not necessarily reflect the boundary conditions. ANSYS CFX overwrites these values using a wall function which attempts to mimic the logarithmic layer and viscous sublayer. These are referred to as the ‘hybrid values’. In the case of a No-Slip boundary condition, the ‘hybrid values’ force the velocity at the wall to be zero whereas the ‘conservative values’ do not. Therefore, the hybrid values were used in this study.

Boundaries that were not specified as domain interfaces and allow for conjugate heat transfer were given a default adiabatic condition. This was used on the majority of the

outside fluid surfaces other than those in contact with the window. It was assumed that once the system comes to steady state, the temperature of the target walls would be the same as the fluid temperature, thereby effectively creating an insulated boundary. This also significantly decreases runtime.

#### 2.6.4. Tetrahedron Elements

The patch independent mesher with tetrahedron shaped elements is recommended by ANSYS for CFD applications and was utilized for this research [16]. This method creates a mesh which is very uniform in size over the entirety of the geometry. The patch dependent mesher provides the benefit of adjusting elements sizes depending upon the geometry. For these complex fluid geometries however, the patch dependent mesher would often over develop the corners of the geometry and under develop the bulk fluid, which is important in this study. Hexahedral shaped elements were also considered for their evenness around boundaries however this type of mesh fails frequently over complex geometries. This is because the meshing program is selective of what surfaces it can create a meshing map over. A surface which can be meshed by hexahedral elements is referred to as being a ‘mappable’ surface. Another problem with hexahedral elements is that they can produce poorly distributed elements in the center of cylindrical geometries. The tetrahedron mesh on the other hand is more robust and does not fail as often. As such, the ANSYS Mesher provides the capability to use the tetrahedron shaped elements over the bulk of the geometry mesh and select specific surfaces to add hexahedral boundary elements to. This function is referred to as ‘Inflation’ and is further explained in section 2.6.5.

### 2.6.5. Boundary Layer Development

If left unrefined, the tetrahedron elements at the boundary layer produce jagged velocity distributions due to their pointed shape. In addition, the wall functions are not applicable at that distance away from the wall. In order to fully develop the boundary layer, the ANSYS meshing program has an Inflation option to create a specified number of boundary layer elements that are hexahedral in shape around a user-selected surface. It is common practice to put at least 10 elements into the boundary layer for full resolution, although more is better. In this study, 15 boundary layer elements are typically used. The thickness of the boundary layer is dictated by a boundary layer growth rate, as well as the value of  $y^+$  (also expressed as  $y^+$ ). This  $y^+$  quantity is a dimensionless number which expresses the distance from the wall to the first node and given as:

$$y^+ = \frac{u_* y}{\nu} \quad (41)$$

$$u_* = \sqrt{\frac{\tau_w}{\rho}} \quad (42)$$

For the SST model, it is common practice to have a  $y^+$  value of approximately 1 and a growth rate of 1.1 to 1.3. The reason for this is the viscous sublayer occurs at  $y^+$  less than 11, so this allows for several nodes to develop the viscous sublayer region. The automatic wall function then overwrites the boundary elements to the boundary condition. For example, with the no-slip condition the velocity is forced to zero at the wall.

As a general rule of thumb, it is important to abide by two general principles when developing a mesh.

1. The distribution from zero velocity at the wall to the fully developed region should be a smooth transition through the entire range of the variable, meaning there should not be any sudden jumps in velocity, temperature, etc.
2. When creating a boundary layer, the largest boundary layer element should be no less than 50% the size of the bulk mesh elements. This means, a smooth transition should exist between the boundary layer and bulk elements.

As shown in Figure 12 a boundary layer mesh is created around a pipe comparable in diameter to the recirculating targets in this study. The  $y^+$  value for the developed boundary is approximately equal to 1, with fifteen layers in the boundary.

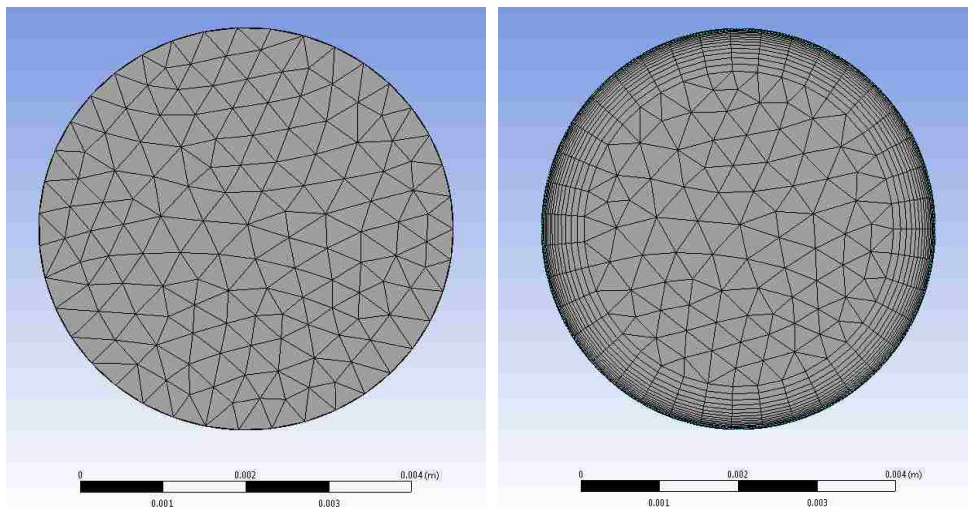


Figure 12: Undeveloped boundary layer (left) and developed boundary layer using Inflation (right)

These two models were then run using identical flow rates. Figure 13 shows a cross-section of the velocity distribution.

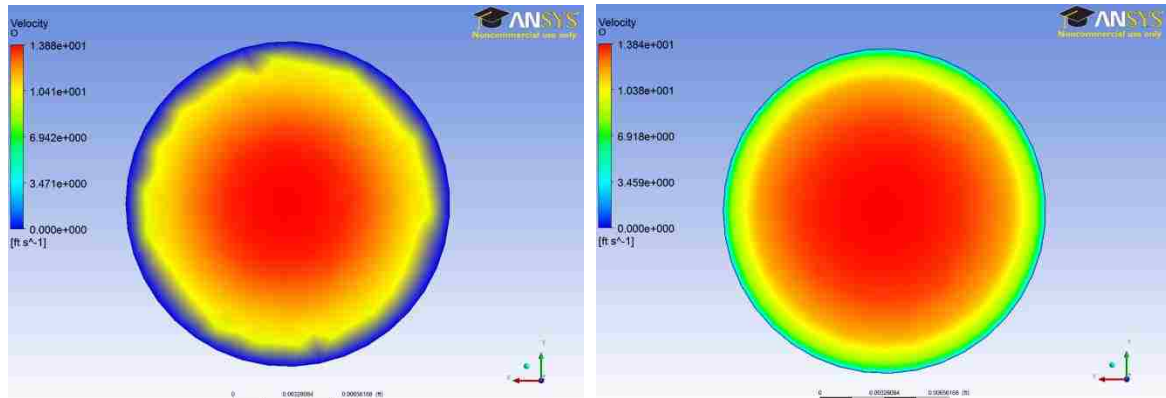


Figure 13: Velocity distribution through pipe without boundary layer (left) and with boundary layer (right)

From Figure 13 it is apparent that the velocity profile for the pipe with the boundary layer elements exhibits a smooth transition moving away from the wall. Furthermore, the  $y^+$  values which result from an undeveloped boundary are outside the range of the wall function. Therefore, it is imperative to use the inflation function when modeling targets to insure accurate results.

### 2.6.6. Proton Beam Heat Implementation

MCNPX outputs a tally sheet with the predicted heat generation rates over a given set of finite volumes. These can either be expressed in cylindrical coordinates as ‘rings’ given by  $\Delta r$  and  $\Delta z$  or in Cartesian coordinates as ‘blocks’ given by  $\Delta x$ ,  $\Delta y$ , and  $\Delta z$ . Using this output tally, an Excel sheet was created which takes the MCNPX output file and creates a table of point-wise heat generation rate data. These points are then imported into ANSYS CFX and applied as volumetric heat generation rates over a specified Subdomain. An independent variable was created in ANSYS CFX so the volumetric heat generation rate can be viewed in

CFX-Post. Figure 14 shows an example of the heat generation distribution using the MCNPX viewer compared to that which is produced in ANSYS CFX.

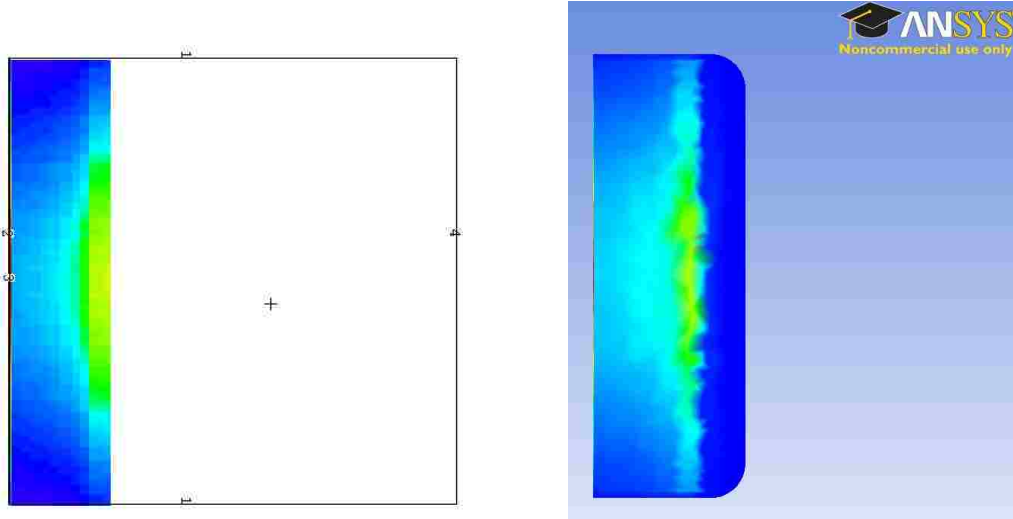


Figure 14: MCNPX heat generation distribution (left) vs. ANSYS CFX heat generation distribution (right)

From Figure 14, it is apparent that although the overall shape and relative distribution remains the same, there are some noticeable differences between the two models due to different types of meshing elements. The MCNPX model is meshed using evenly spaced cuboids and produces a very symmetric cross-sectional distribution. In contrast, ANSYS CFX uses tetrahedral shaped meshing elements which cannot be evenly cut by a plane. This meaning, the distributions are comprised of elements that are not at a consistent axial location. Another difference is that the MCNPX model does not color areas of zero heat generation as blue like the ANSYS CFX model. This is why the MCNPX distribution stops after the Bragg peak whereas the ANSYS CFX distribution continues to the bottom of the target chamber.

The effect of these differences, while small, is important to understand. Due to the differences in the discretization methods used in the two programs, the shape of the Bragg peak can become skewed and therefore the heat generation distribution is not entirely accurate when being applied. Figure 15 shows a graph of the heat generation rate between both models shown in Figure 14, for a line that runs axially through the center of each distribution.

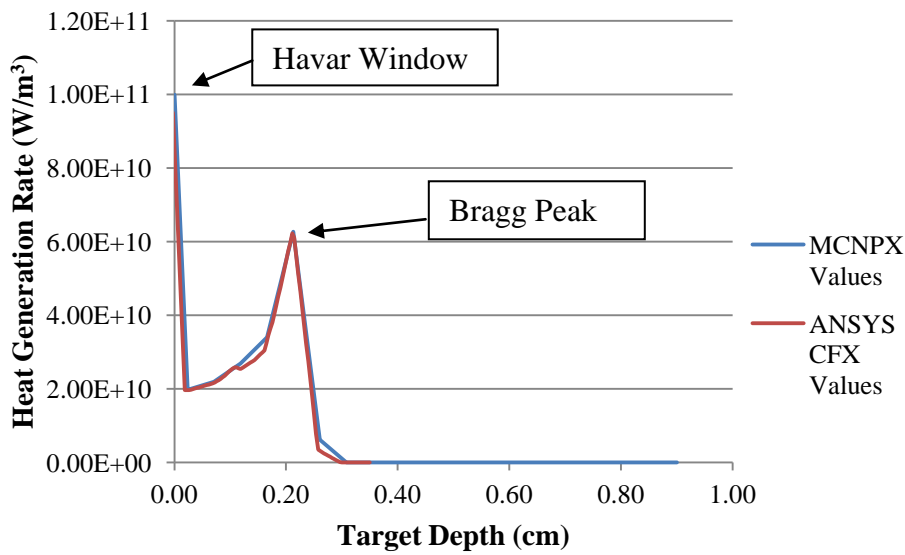


Figure 15: Heat generation rate through the center of the distributions shown in Figure 14

As shown from Figure 15, there are noticeable differences between the MCNPX and ANSYS CFX values; however these differences are small in comparison to overall values and therefore were determined to be acceptable for this study.

## Chapter 3 - Target Designs and Analysis

The evolution of the recirculating target design is presented in this chapter. The analysis will initially be a comparison of models developed in ANSYS CFX. Further analysis will be provided for the final target configuration.

### 3.1. Design Considerations

The limiting criteria when evaluating candidate target designs was chosen to be that the maximum temperature inside the system does not surpass the saturation temperature. For all cases considered here, this corresponds to a temperature of 444.6 °F and a pressure of 400 psi. This is standard system operating pressure. This criterion was chosen to prevent vapor bubbles traveling downstream, potentially leading to pump failure.

It was decided that small amounts of local subcooled boiling on the window would be allowed since these bubbles would likely collapse before reaching the pump in such a highly subcooled environment. In addition, the selected pump is capable of accommodating up to 20% by volume vapor. As such, several studies were done which ignored the local window hotspot surpassing the saturation temperature and focused primarily on the bulk fluid at the Bragg peak reaching saturation as the limiting criteria. This leads to another positional limiting criterion which is the fluid/window interface reaching critical heat flux (CHF). Several attempts were made to quantify critical heat flux in flow boiling systems of this type. However, due to the lack of applicable correlations these were only rough estimates and could not be used with confidence. This is explained further in section 3.6.



## 3.2. Recirculating Target 1 (RT-1)

### 3.2.1. Design

The first design studied was a prototype designed and fabricated by Bruce Technologies Inc. Coolant enters a distribution manifold within the target through two symmetrically located main channels. From the distribution manifold the coolant passes through six 1/16” diameter jetting channels which direct fluid at a 30° angle toward the center of the target window [1]. The target fluid flows through a central target chamber and exits the back of the target body. It was hoped this design would provide maximum cooling to the window since that has traditionally been the position of maximum temperature and has the highest probability of target failure.



Figure 16: RT-1 assembled target [1]

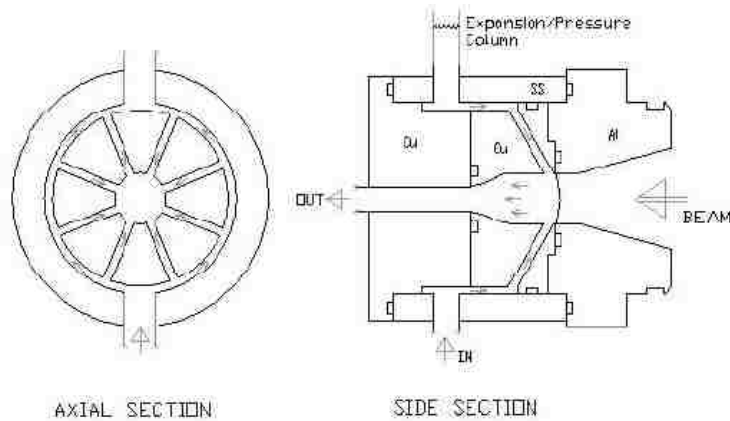


Figure 17: Drawing of RT-1 [1]

### 3.2.2. ANSYS Target Model: RT-1

The target was modeled in ANSYS CFX using the shear stress transport turbulence model. The only difference between the ANSYS CFX model and the fabricated target was that the outlet tube was modified so it was the same diameter as the bottom of the target chamber, thus eliminating the contraction piece. This was done to reduce the pressure drop and simplify the design. Boundary layer elements were added to all applicable surfaces and unless otherwise stated, the same approach was used in all ANSYS target models. The following figures show the geometry, mesh, velocity streamlines, and velocity distribution.

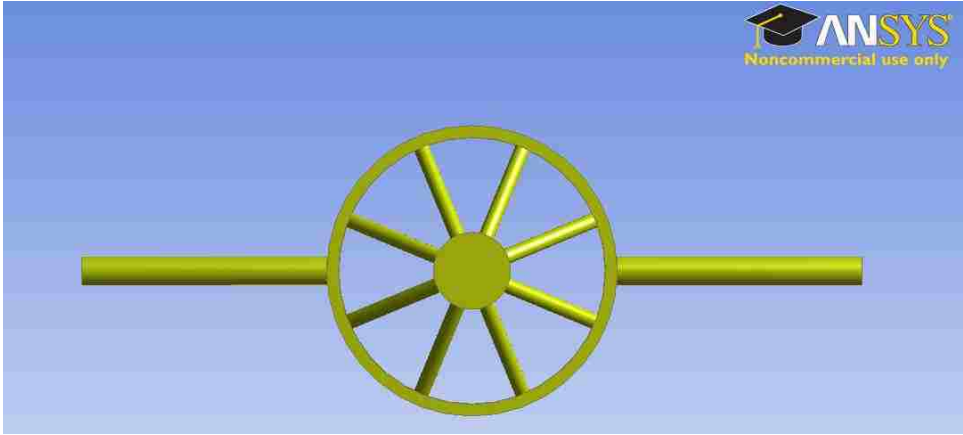


Figure 18: RT-1 extracted fluid, overhead view

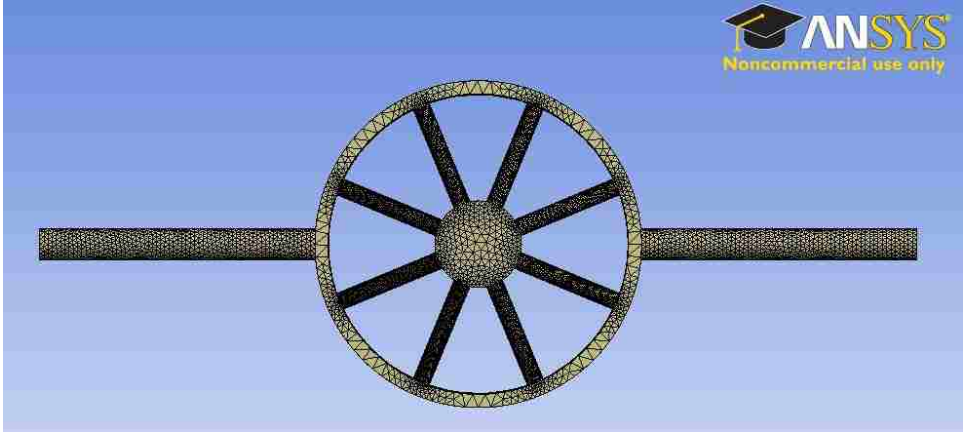


Figure 19: RT-1 Mesh

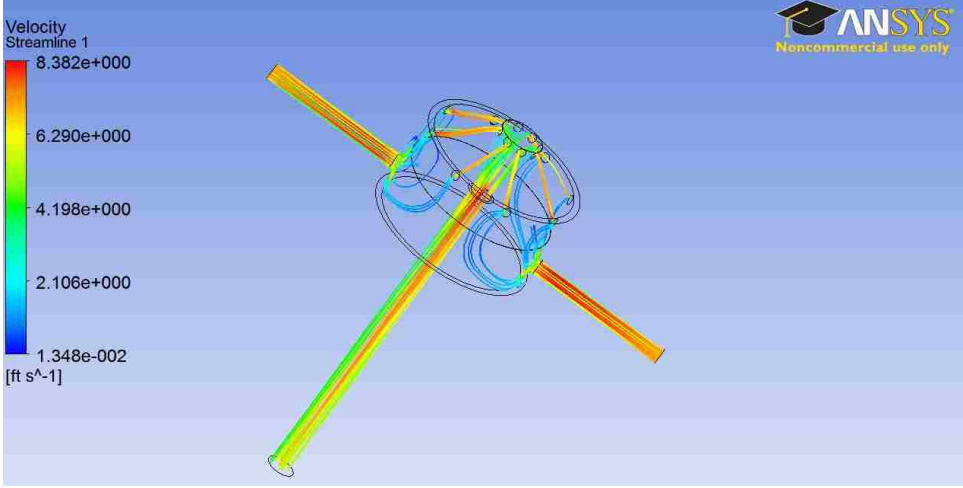


Figure 20: RT-1 velocity streamlines, flow rate: 0.1 lb/s

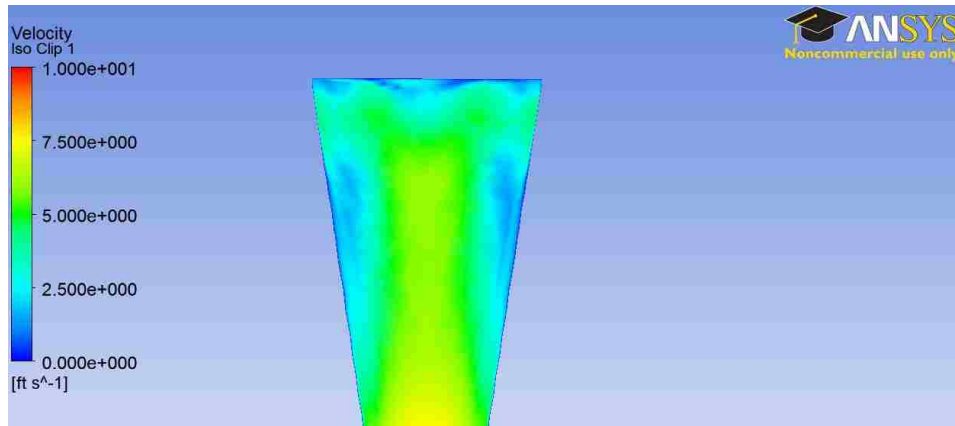


Figure 21: RT-1 velocity distribution through cross-section of target chamber, flow rate: 0.1 lb/s

Figure 20 shows the velocity streamlines through RT-1. Ideally, there would be uniform flow through each of the six jetting channels. However, given that there are only two main coolant inlets, channels which are closest to the inlet have the highest flow rate.

### 3.2.3. RT-1 Pressure Drop and Inlet Temperature

The RT-1 model was run between  $0.1 - 0.2 \frac{lb}{s}$  to create a pressure drop curve. The pressure drop across the target was taken as the average inlet pressure minus the average outlet pressure. This was then used in combination with the heat exchanger and pump pressure drop curves to calculate the system flow rate. The total system flow rate for the RT-1 target was determined to be  $0.1896 \frac{lb}{s}$ . An experimental pressure drop curve was created in prior work, however only flow rates below  $0.08 \frac{lb}{s}$  were measured [1]. Therefore, no comparable data is available.

Table 5: RT-1 pressure drop and corresponding system flow rate

Mass Flow Rate (lb/s)	Pressure Drop (psi)
0.10	0.72
0.12	1.00
0.14	1.32
0.16	1.69
0.18	2.11
0.20	2.57
<b>System Flow Rate (lb/s):</b>	<b>0.1896</b>

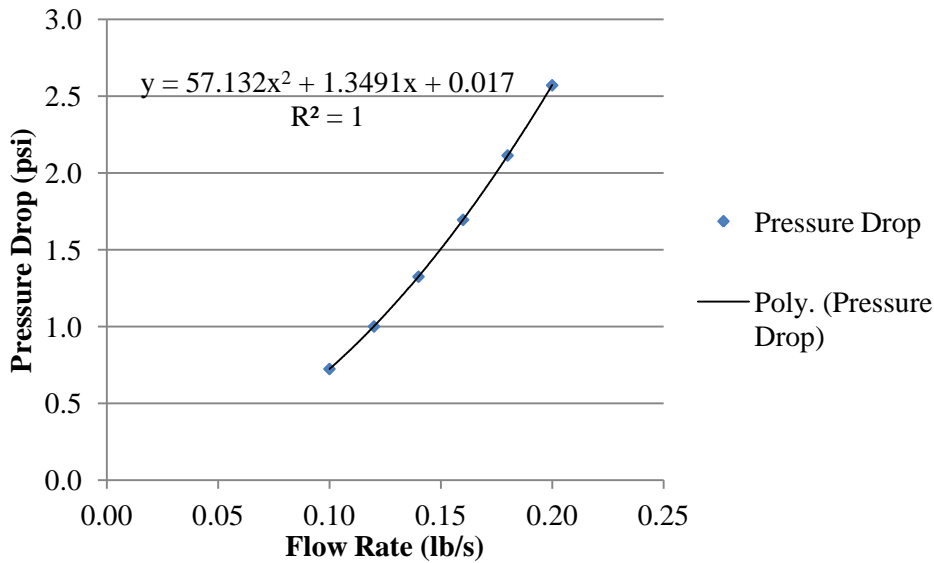


Figure 22: RT-1 pressure drop curve

For a total system flow rate of  $0.1896 \frac{lb}{s}$ , a total heat input of 2.7 kW and specified heat exchanger characteristics, the inlet temperature to the target was calculated to be  $101.65^{\circ}F$ . This inlet temperature and system flow rate is then used as the starting point in the ANSYS CFX model of the heated target.

### 3.2.4. RT-1 Heated Model

Figure 23 shows the temperature distribution predicted through the center of the target chamber. This trial was run using a 27 MeV, 100  $\mu$ A beam resulting in a total of 2.7 kW of heat added to the target. This is one of two designs which were solely intended to use 27 MeV protons.

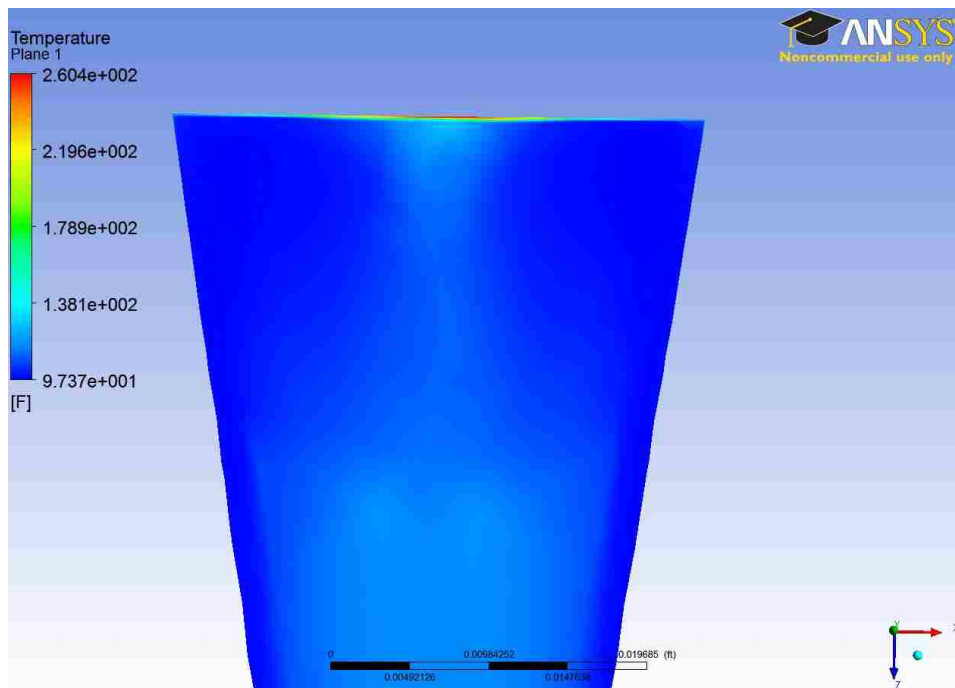


Figure 23: RT-1 temperature distribution through a cross-section of the target chamber

### 3.2.5. RT-1 Observations and Analysis

There are two main disadvantages to this design:

1. The diameter of the target chamber is 10mm at the top and just over 7mm in diameter at the stopping distance of 27 MeV protons in water. Therefore, the proton beam is restricted to only 7mm in diameter even though the collimator can

create a beam up to 10mm in diameter. A larger beam is more desirable because it distributes the beam's energy over a broader area.

2. The six cooling jets create a stagnation point at the center of the window. This is also the location of maximum heat generation within the window and ultimately limits RT-1. Figure 24 explicitly shows this stagnation point, in which a surface velocity streamline is imposed over the same temperature distribution plane.

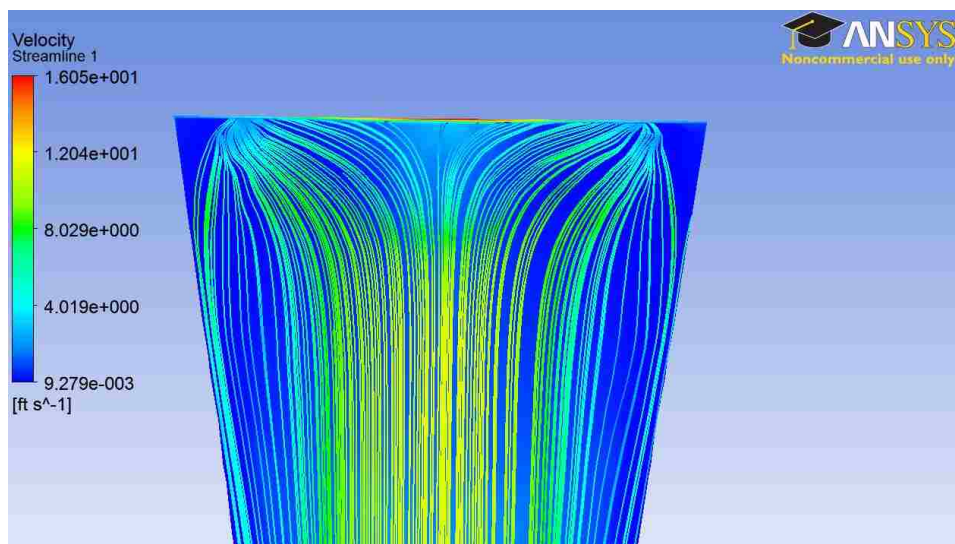


Figure 24: RT-1 stagnation point location

### 3.3. RT-2

#### 3.3.1. Design

The goal of this design was to switch the direction of flow such that fluid would now flow parallel to the window as opposed to being directed normal to it. In order to maintain adequate cooling at the Bragg peak, one hundred and seventeen 1/16” channels are used to direct flow to the desired hotspot locations. Thirty-nine channels direct fluid at the window

and the remaining seventy-eight direct water across the main target chamber. These channels are fed through a primary inlet tube with the fluid exiting the target through channels on the opposite side of the target chamber.

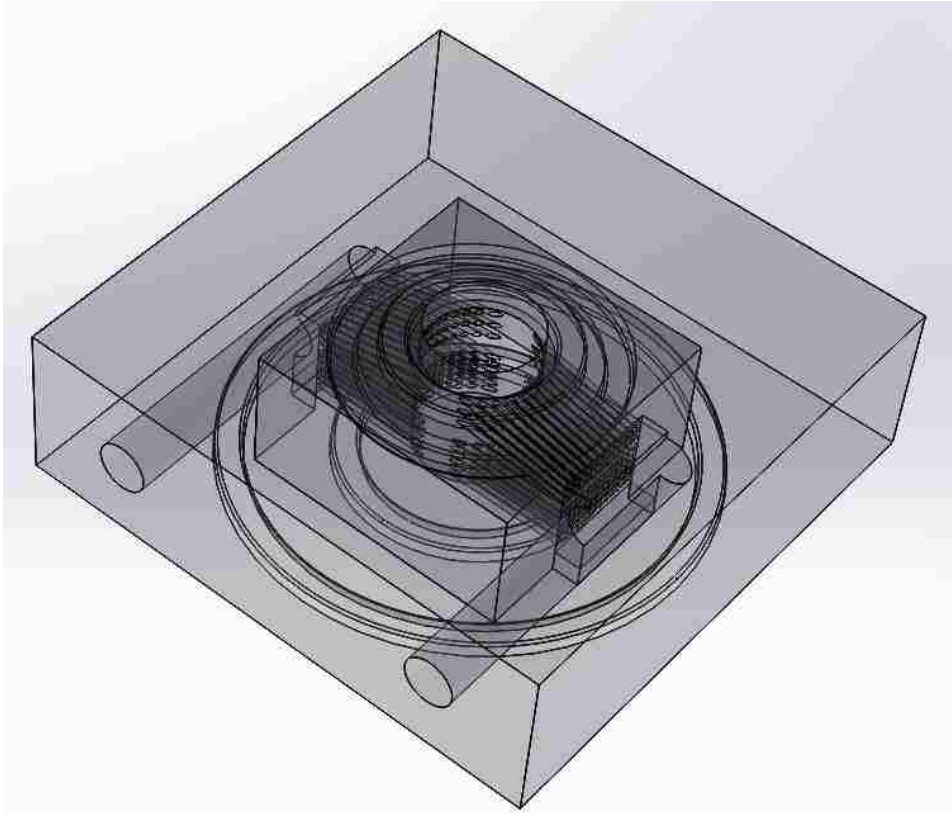


Figure 25: RT-2

Figure 25 shows the current version of this target design. Since it was never considered for fabrication, drill holes, O-rings and the upper holding plate were not included in the SolidWorks model.

### 3.3.2. ANSYS Target Model: RT-2

The number of inlet and outlet channels surpassed the limit of the ANSYS meshing program and boundary layer nodes could not be applied to the 1/16” channels. As such,



only the inlet tube, outlet tube, and target chamber were given a developed boundary layer. The following figures show the geometry, mesh, velocity streamlines, and velocity distribution.

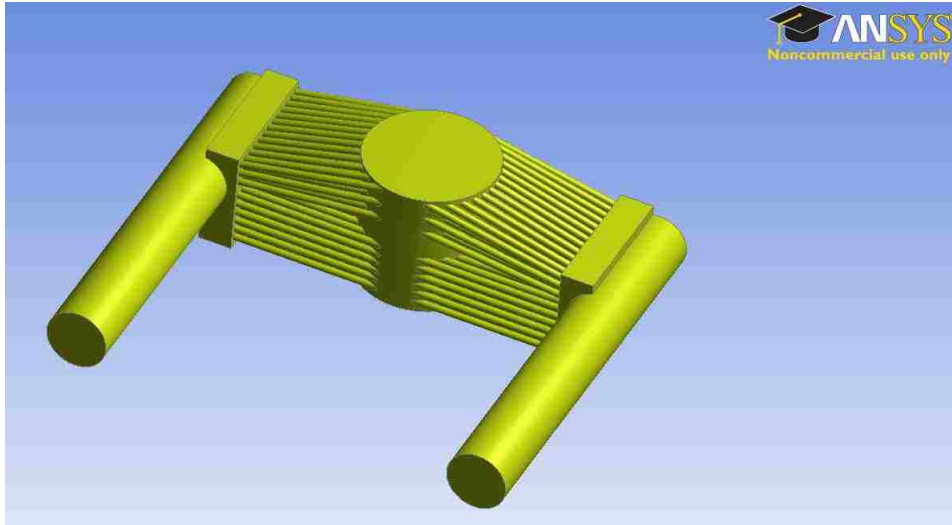


Figure 26: RT-2 extracted fluid

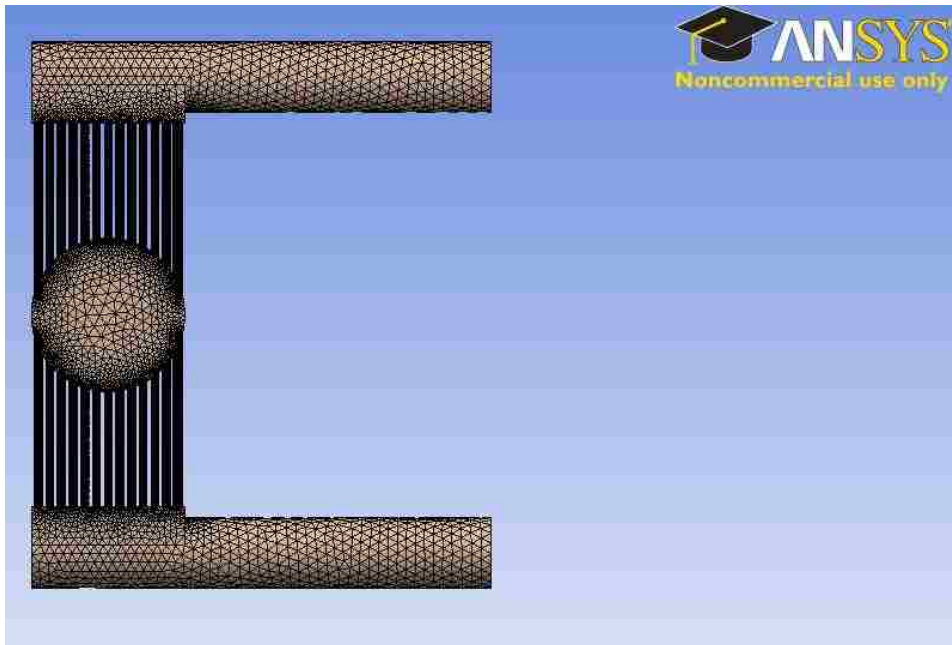


Figure 27: RT-2 mesh, overhead view

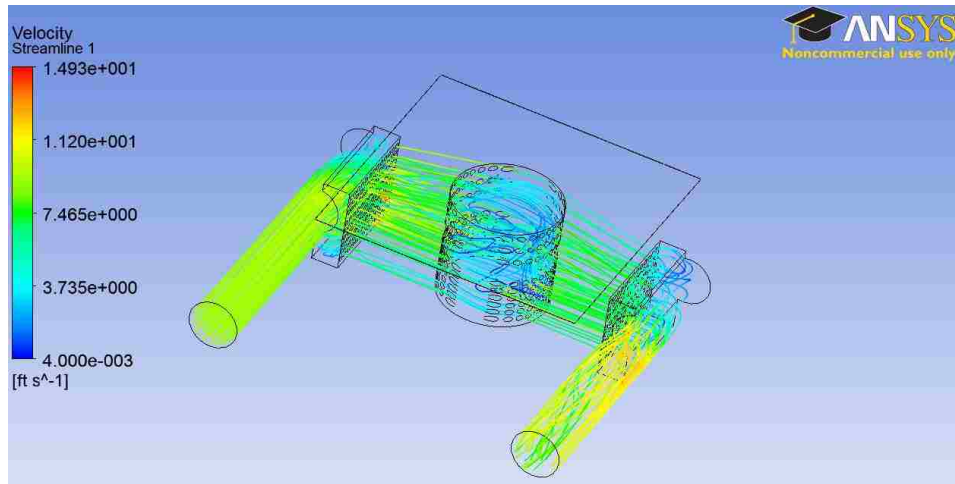


Figure 28: RT-2 velocity streamlines, flow rate: 0.1 lb/s

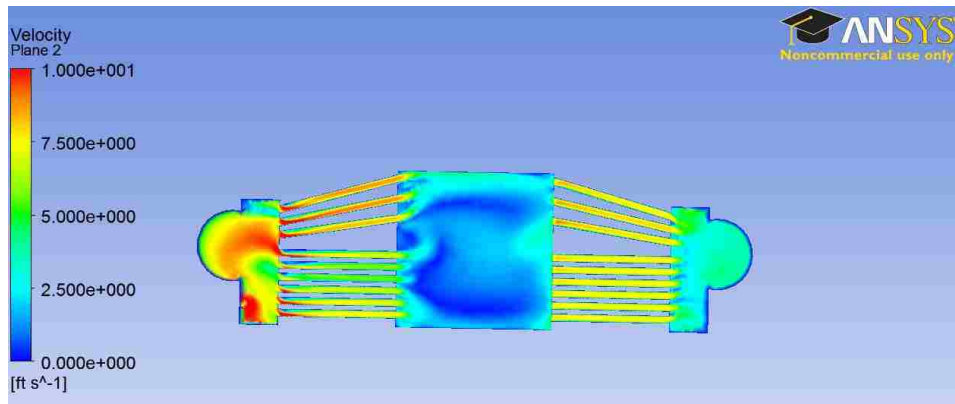


Figure 29: RT-2 velocity distribution through cross-section of target chamber, flow rate: 0.1 lb/s

Figure 28 shows the velocity streamlines through the target. A few things should be highlighted. First, the beam-strike occurs at the top of the circular target chamber. The chamber diameter is 10mm, so the maximum size beam can be used. Second the inlet and outlet tubes were placed higher such that more flow would be directed into the channels pointing toward the window. This was done to provide more cooling to the window since that was the limiting factor in RT-1. Third, the target chamber was made deep enough to accommodate 27 MeV protons.

### 3.3.3. RT-2 Pressure Drop and Inlet Temperature

The RT-2 model was run between  $0.1 - 0.2 \frac{lb}{s}$  to create a pressure drop curve. Again, the target pressure drop was taken as the average inlet pressure minus the average outlet pressure. This was then used in combination with the heat exchanger and pump pressure drop curves to calculate the system flow rate. The total system flow rate for the RT-2 target was determined to be  $0.1850 \frac{lb}{s}$ .

Table 6: RT-2 pressure drop and corresponding system flow rate

Mass Flow Rate (lb/s)	Pressure Drop (psi)
0.10	2.40
0.14	4.29
0.16	5.40
0.18	6.54
0.20	7.96
<b>System Flow Rate (lb/s): 0.1850</b>	

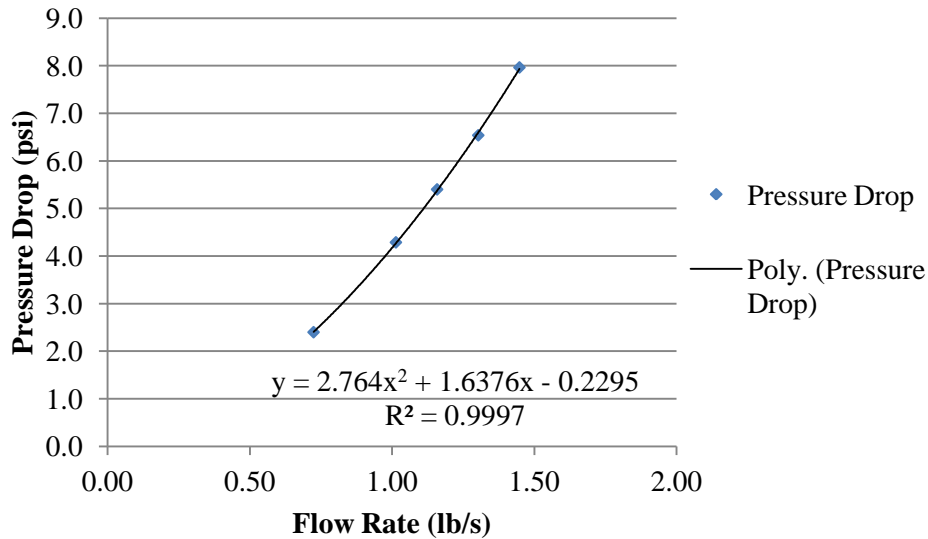


Figure 30: RT-2 pressure drop curve

For a total system flow rate of  $0.1850 \frac{lb}{s}$ , a total heat input of 2.7 kW, and specified heat exchanger characteristics, the inlet temperature to the target was calculated to be 102.89 °F. This inlet temperature and system flow rate is then used as the starting point in the ANSYS CFX model of the heated target.

### 3.3.4. RT-2 Heated Model

RT-2 was run in ANSYS using the same 27 MeV, 100  $\mu$ A beam for a total heat input of 2.7 kW. The temperature distribution is illustrated in Figure 31.

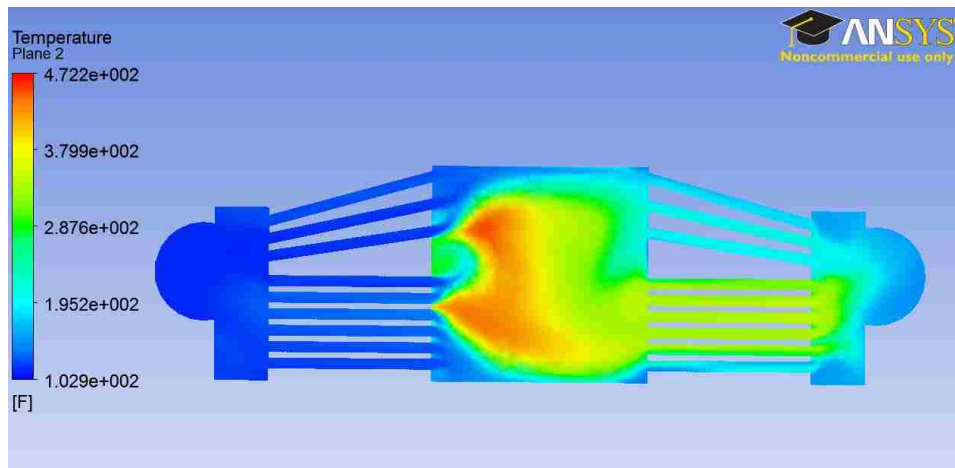


Figure 31: RT-2 temperature distribution through a cross-section of the target chamber

### 3.3.5. RT-2 Observations and Analysis

The maximum temperature of 472.2 °F in Figure 31 is slightly above the saturation temperature of 444.6 °F. ANSYS CFX does not have the ability to simulate two-phase flow conditions, and as a result these simulations do not accurately reflect the true target behavior. However, a number of conclusions can still be drawn from these simulations:

- There exists large eddies through the center of the target chamber. This causes flow to stagnate and heat up past the acceptable temperature.
- The reason for this stagnation is attributable to the flow having no clearly defined flow path after exiting the jets which directs fluid toward the Bragg peak.

As some flow is directed upward toward the window, while the rest is directed at the Bragg peak, this leaves a gap in which there is little to no flow and ultimately causes unwanted stagnation. While this design failed, it did result in enhanced cooling of the target window. Therefore it can be concluded that moving the direction of flow from normal to the window to parallel to the window is a promising design change.

## 3.4. RT-3

### 3.4.1. Design

The goal of RT-3 was to reduce the complexity of the fluid path such that there would only be one main channel for fluid flow across the window and Bragg peak areas. From RT-2, it was learned that diverting the flow to two locations would lead to stagnation areas. The shape of the target chamber and inlet channel in RT-3 caused flow to swirl around the chamber in a circular motion, creating a smooth flow path. This is an improvement from RT-2 where target fluid had no orderly direction to flow through the chamber. The target chamber is deep enough to accommodate 27 MeV protons. However, it was found that using 14 MeV protons proved more advantageous because the Bragg peak was located in an area of higher flow rate.

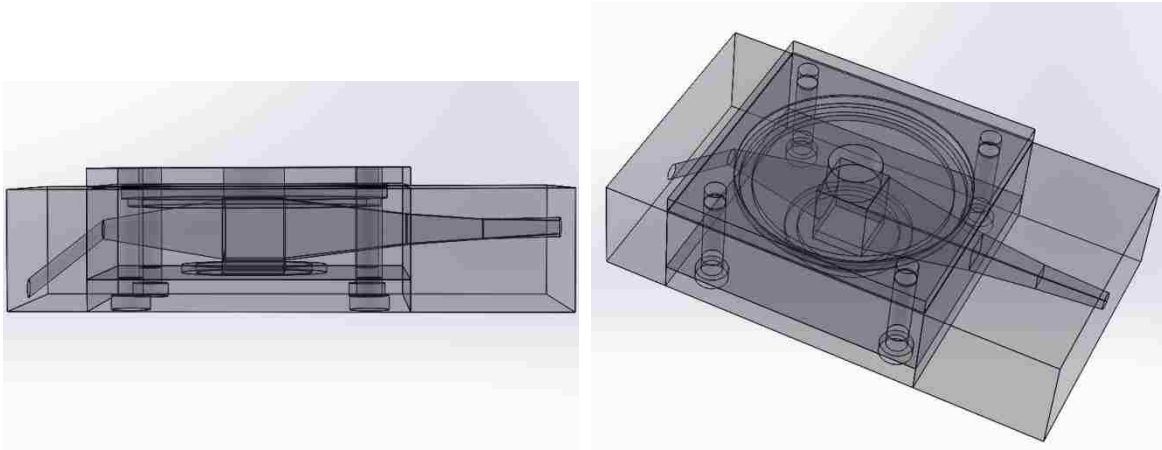


Figure 32: RT-3

Figure 32 shows the current RT-3 target design. Several studies were done to optimize the inlet angle so that there was a balance of cooling to the window and Bragg peak. This design contains some of the necessary O-ring groves and bolt locations; however there were fabrication issues which will be discussed later.

#### 3.4.2. ANSYS Target Model: RT-3

Since the design was relatively simple, all faces were given boundary layer elements. The following figures show the extracted fluid, mesh, velocity streamlines, and velocity distribution.

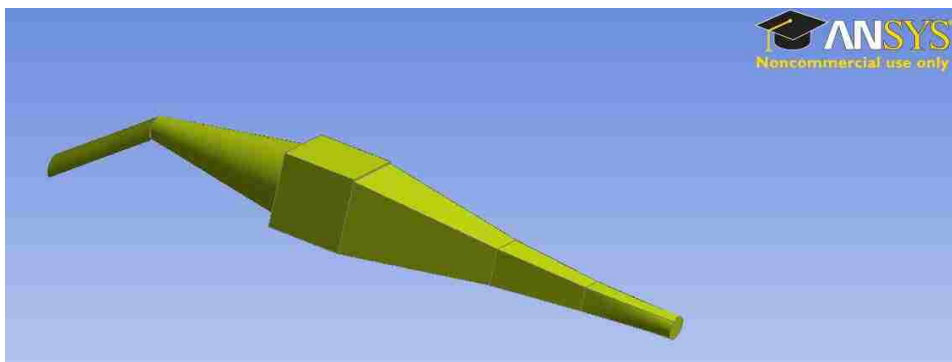


Figure 33: RT-3 extracted fluid



Figure 34: RT-3 mesh

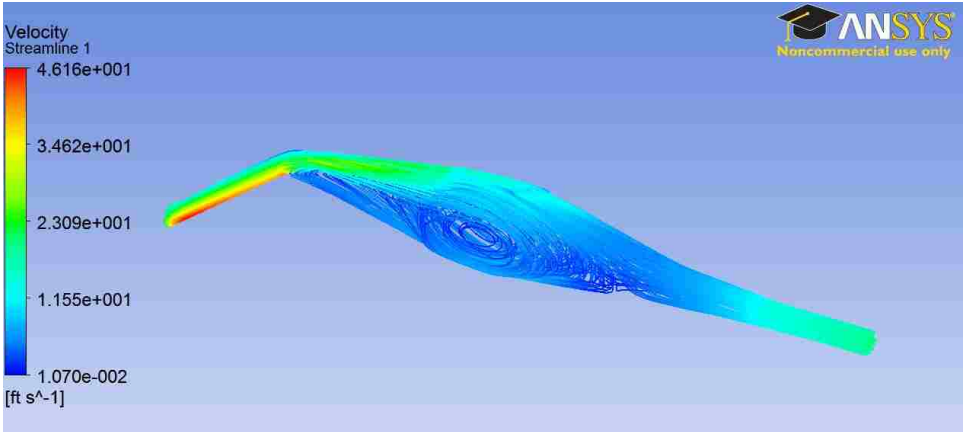


Figure 35: RT-3 velocity streamlines, flow rate 0.1 lb/s

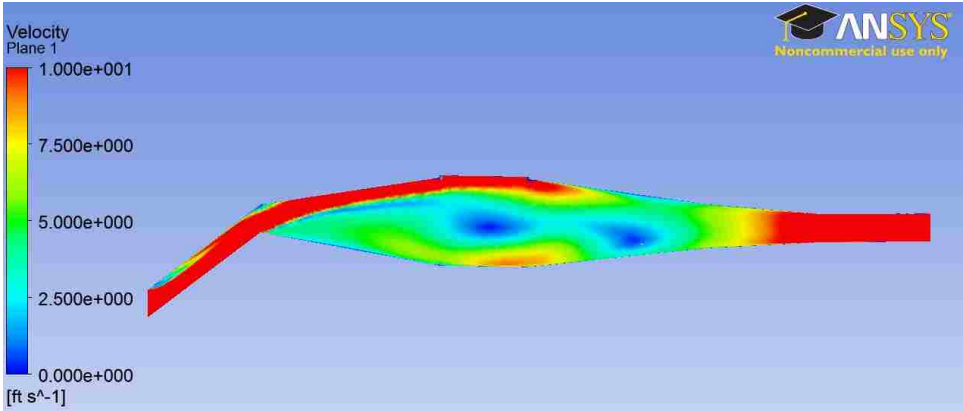


Figure 36: RT-3 velocity distribution through cross-section of target, flow rate: 0.1 lb/s

There are several important observations which need to be made about RT-3. First, Figure 36 shows the magnitude of the velocity, which is why it is always positive. In reality, the flow circulates around the chamber as shown in the streamlines. The amount of cooling at the window in this design is far superior to RT-1 and RT-2, which gives it a distinct advantage. The circulating flow also results in a stagnation point at the center of the target which will need to be taken into consideration when selecting the proton energy.

### 3.4.3. RT-3 Pressure Drop and Inlet Temperature

The RT-3 model was run between  $0.1 - 0.2 \frac{lb}{s}$  to create a pressure drop curve. This was then used in combination with the heat exchanger and pump pressure drop curves to calculate the system flow rate. The total system flow rate for the RT-3 target was determined to be  $0.1707 \frac{lb}{s}$ .

Table 7: RT-3 pressure drop and corresponding system flow rate

Mass Flow Rate (lb/s)	Pressure Drop (psi)
0.10	7.92
0.12	11.27
0.14	15.26
0.16	19.83
0.18	24.98
0.20	30.80
<b>System Flow Rate (lb/s):</b>	<b>0.1707</b>



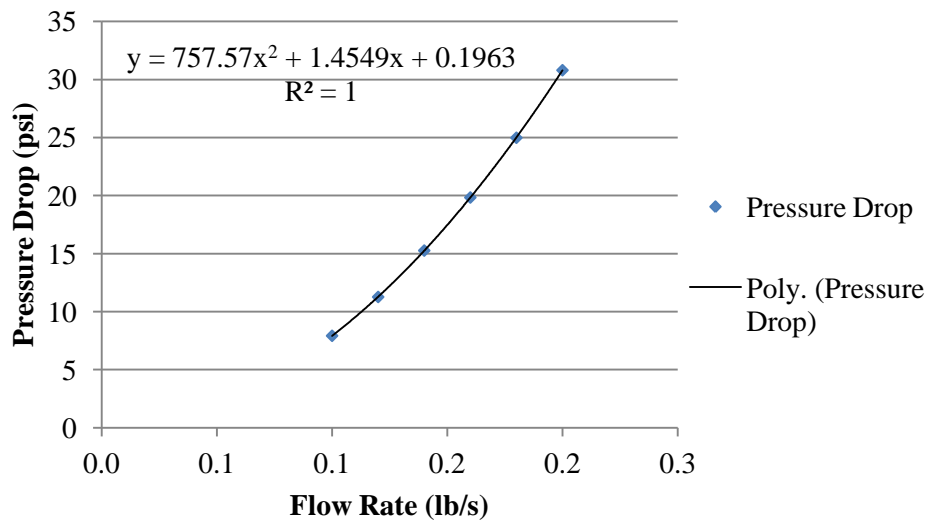


Figure 37: RT-3 pressure drop curve

For a total system flow rate of  $0.1707 \frac{lb}{s}$ , a total heat input of 2.7 kW, and specified heat exchanger characteristics, the inlet temperature to the target was calculated to be 104.59 °F. This inlet temperature and system flow rate is then used as the starting point in the ANSYS CFX model of the heated target.

#### 3.4.4. RT-3 Heated Model

RT-3 was run in ANSYS CFX using a 14 MeV, 192.86  $\mu$ A beam for a total heat input of 2.7 kW. This beam current was chosen with the sole purpose of producing the same total heat input as RT-1 and RT-2. 14 MeV protons were selected because their stopping distance places the Bragg Peak above the stagnation point in the center of the target.

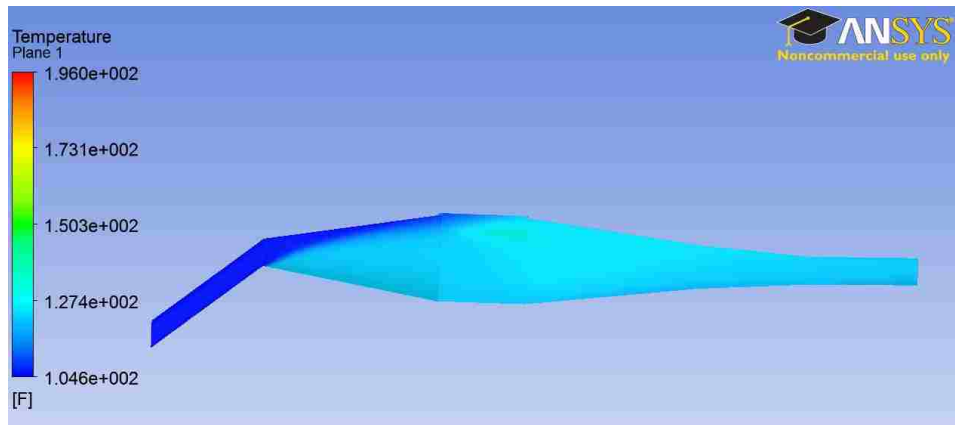


Figure 38: RT-3 temperature distribution

### 3.4.5. RT-3 Observations and Analysis

From Figure 38 it is apparent that the maximum temperature of 196.0 °F is well below the saturation temperature despite having the same total heat input as RT-1 and RT-2. This is attributable to the high flow across the window which creates a very thin boundary layer and does an excellent job cooling the window. There are two main problems with this design:

- An attempt was made to fabricate this design. However, due to the undercut required for the central target piece, fabrication of this design was either turned down by metal shops or would have required special machinery.
- While this target is effective for 14 MeV protons, the Bragg Peak for 27 MeV protons occurs almost exactly at the stagnation point in the center of the target chamber. Therefore, the large target chamber is essentially extra volume without the flexibility to vary proton energies. Figure 39 shows the temperature distribution when using 27 MeV protons. The 2D velocity streamlines are also shown. As expected, a new hotspot occurs at the stagnation point.

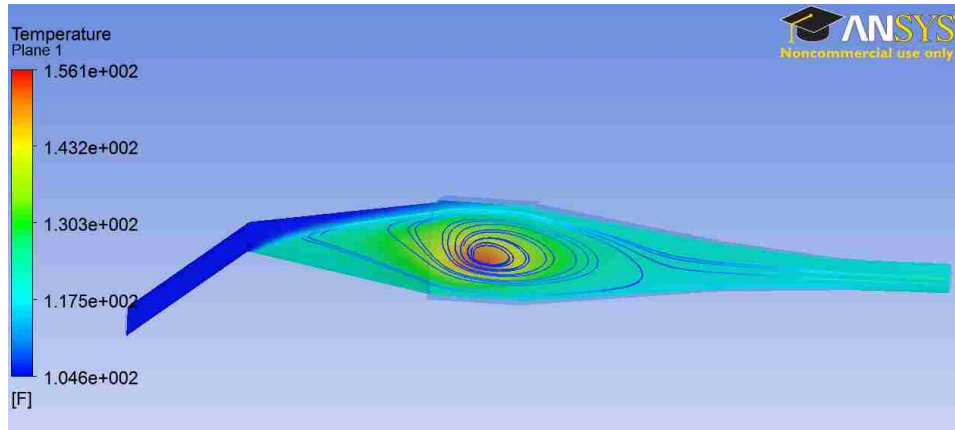


Figure 39: RT-3 velocity streamlines on top of the temperature distribution using 27 MeV protons

## 3.5. RT-4

### 3.5.1. Design

The goal of RT-4 was to improve the fabricability of the target while maintaining adequate cooling and low system volume. This involved designing a target such that no undercut was required during fabrication and breaking the target into multiple sections which could be bolted together. It is important to keep the angled entrance, as it focuses flow on the window. Since 14 MeV protons are more efficient than 27 MeV protons on a per kW basis for the production of  $^{18}\text{F}$ , this design was only made deep enough to accommodate these lower energy protons. As such, this eliminated the circular flow pattern seen in RT-3. Instead, a unique flow pattern is seen in which there are two parallel helical flows that develop after the expansion piece. This also does an excellent job transferring heat away from both the window-fluid interface and the Bragg peak hotspots.

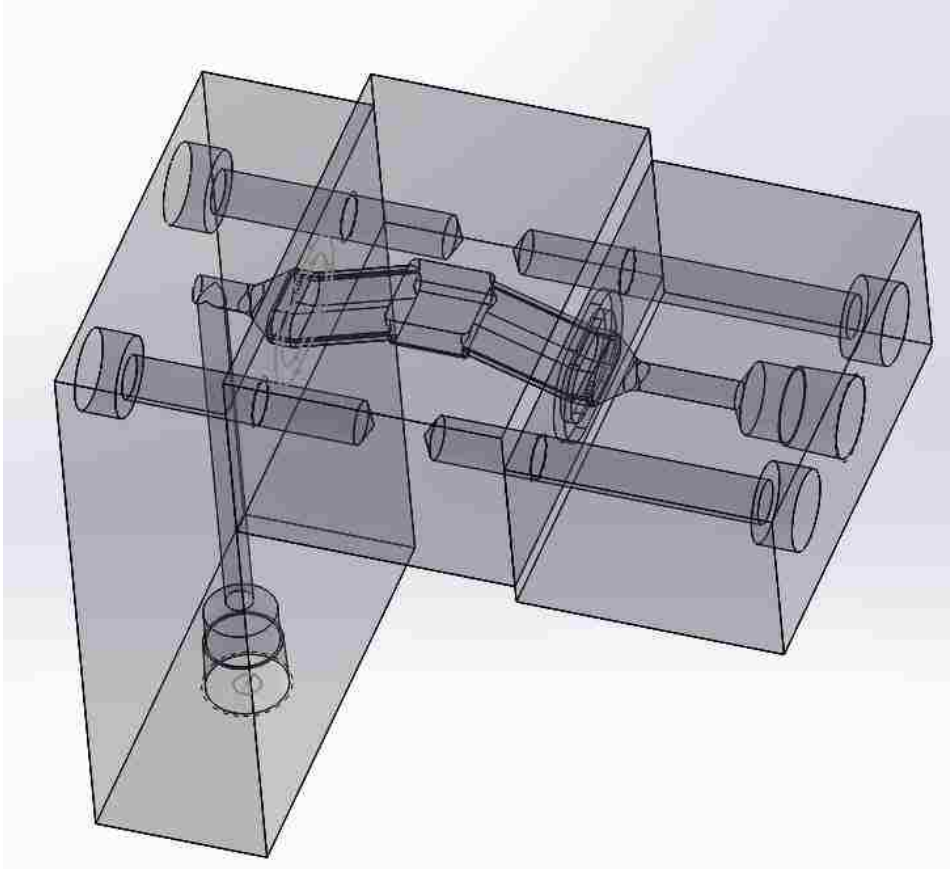


Figure 40: RT-4

As shown in Figure 40, flow enters the target expansion piece through a 90 degree elbow. The flow then traverses the target, and is then directed down and out of the target body. All necessary bolt locations, O-ring grooves, and connector pieces are shown.

### 3.5.2. ANSYS Target Model: RT-4

There were a number of smaller faces on this design which are not ‘mappable’ and therefore boundary layer elements could not be applied to them. The majority of the large faces were mappable, including the entire target chamber. The target chamber is effectively a 10x10mm rectangle which accommodates the largest diameter beam size considered.

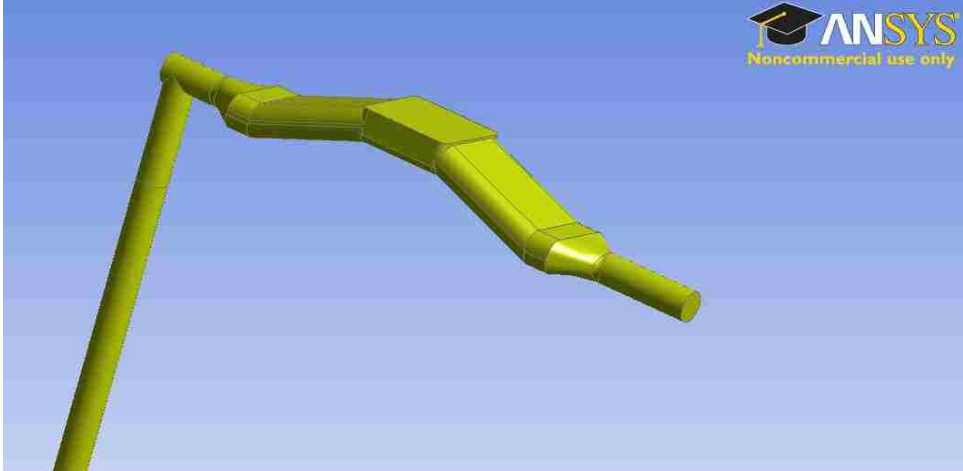


Figure 41: RT-4 extracted fluid

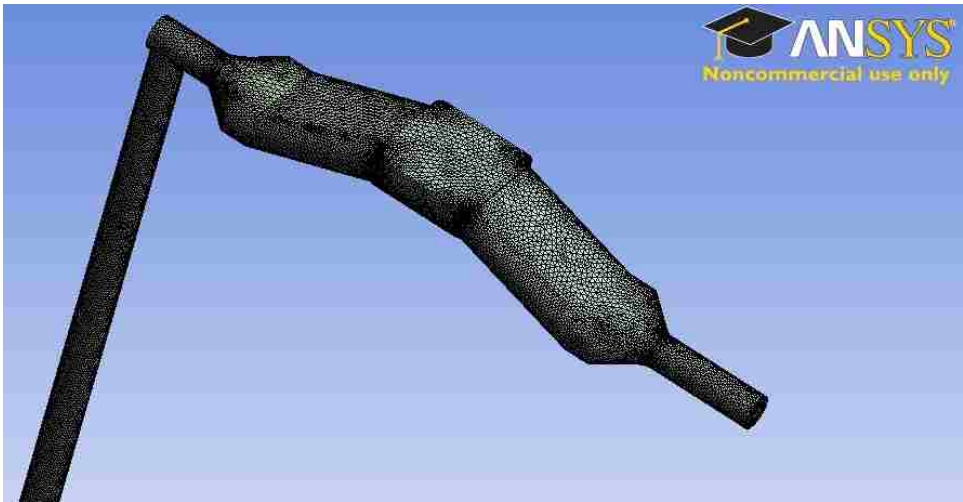


Figure 42: RT-4 mesh

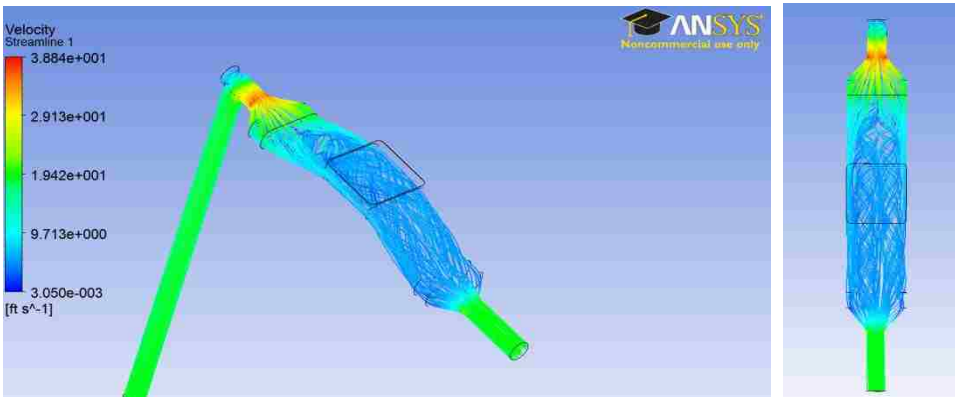


Figure 43: RT-4 velocity streamlines

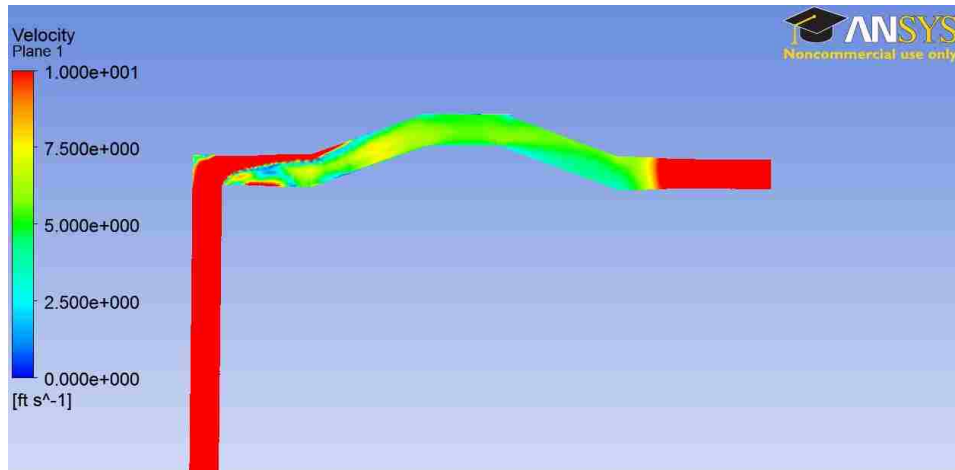


Figure 44: RT-4 velocity distribution

Several important observations can be made regarding RT-4. First, In addition to being convenient for fabrication, the sharp elbow is also crucial in forming the unique flow pattern seen in the target. A study was done which varied the length of the elbow from the expansion piece. Since the sharp elbow is vital to the system, a long inlet tube was used to promote fully developed flow. Second, the fluid velocity across the window is slower than in RT- 3. This is a decline in performance however it is still significantly better than RT-1 and RT-2.

### 3.5.3. RT-4 Pressure Drop and Inlet Temperature

The RT-4 model was run between  $0.04 - 0.2 \frac{lb}{s}$  to create a pressure drop curve. This was then used in combination with the heat exchanger and pump pressure drop curves to calculate the system flow rate. The total system flow rate for the RT-4 target was determined to be  $0.1713 \frac{lb}{s}$ .

Table 8: RT-4 pressure drop and corresponding system flow rate

Mass Flow Rate (lb/s)	Pressure Drop (psi)
0.11	7.40
0.13	10.52
0.15	14.35
0.20	22.49
0.22	28.82
0.18	18.60
0.07	2.87
0.04	1.35
<b>System Flow Rate (lb/s):</b>	<b>0.1713</b>

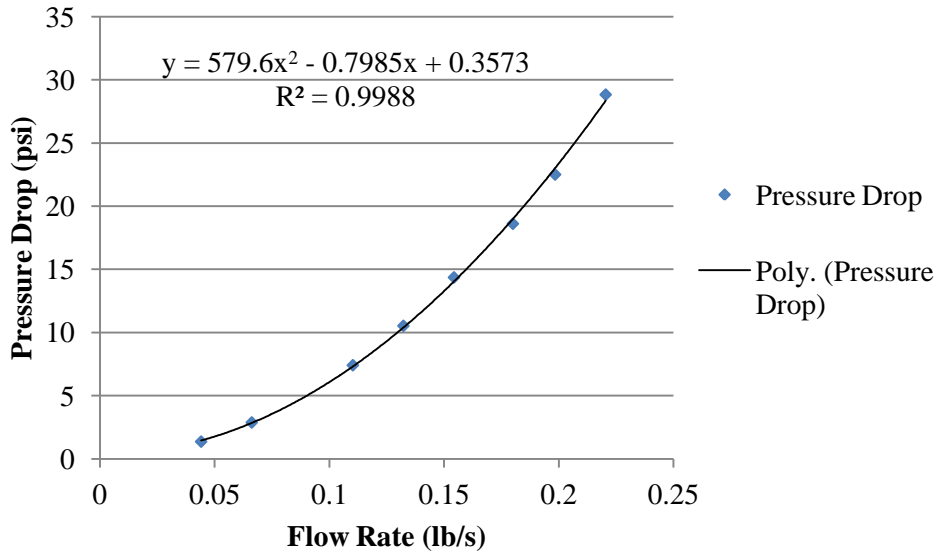


Figure 45: RT-4 pressure drop curve

For a total system flow rate of  $0.1713 \frac{lb}{s}$ , a total heat input of 2.7 kW, and specified heat exchanger characteristics, the inlet temperature to the target was calculated to be 104.54 °F. This inlet temperature and system flow rate is then used as the starting point in the ANSYS CFX model of the heated target.

### 3.5.4. RT-4 Heated Model

RT-4 was run in ANSYS using a 14 MeV, 192.86  $\mu\text{A}$  beam for a total heat input of 2.7 kW. Again, this beam current was chosen with the sole purpose of producing the same total heat input as RT-1 and RT-2. 14 MeV protons were selected because the target chamber is only deep enough for this energy.

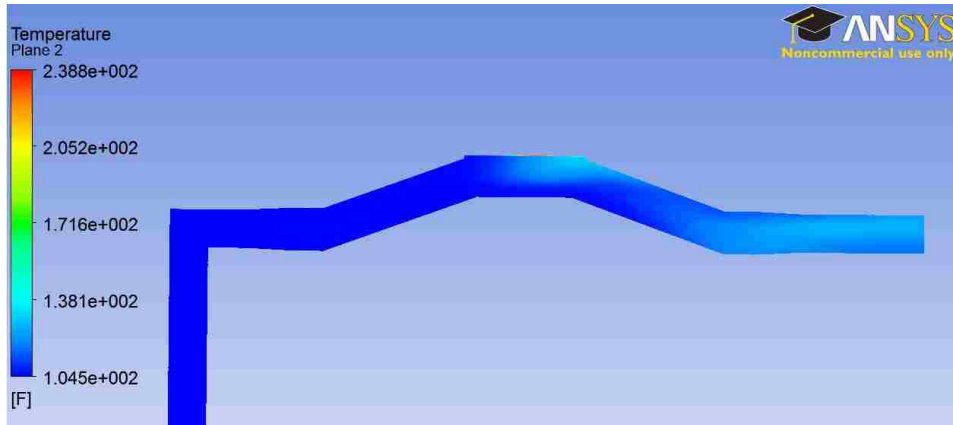


Figure 46: RT-4 temperature distribution

### 3.5.5. RT-4 Observations and Analysis

Figure 46 shows the temperature distribution through the center of RT-4. Compared to RT-3 there is a slight decrease in performance. Like RT-1 and RT-3, the position of maximum temperature occurs at the window-fluid interface and is predicted to be 238.8  $^{\circ}\text{F}$ .

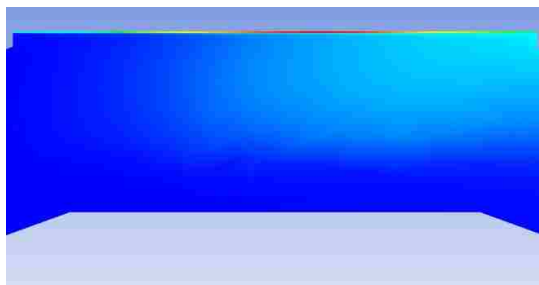


Figure 47: RT-4 window hotspot temperature distribution close-up



There are no critical design flaws associated with this geometry, although RT-3 provides superior cooling for the window. Consequently, it was concluded that RT-4 was the best of the four options.

### 3.5.6. Verification through Fluent

Since the flow pattern exhibited in RT-4 was so unique, additional verification was desired. This was done by testing RT-4 using Fluent 13.0, another common CFD package. Similar initial conditions, boundary conditions, mesh, and fluid models were used as in the CFX model. The same post-processing software is also used. The following figures show the streamlines and velocity distribution for the RT-4 model when using Fluent.

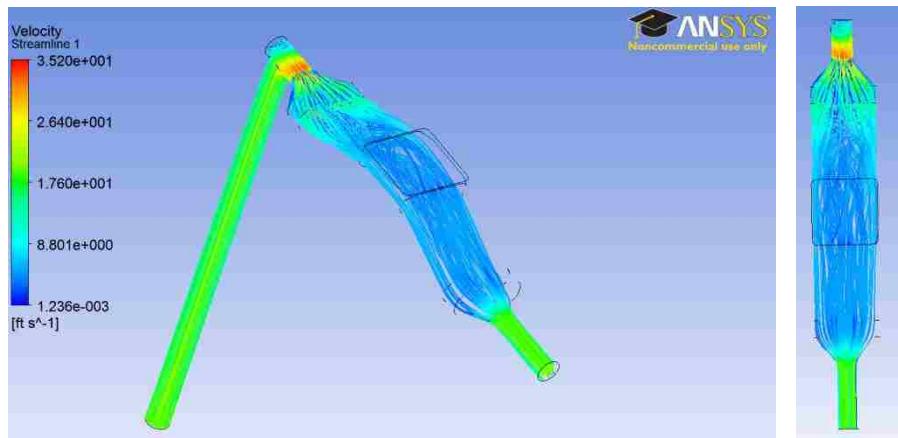


Figure 48: RT-4 velocity streamlines using Fluent

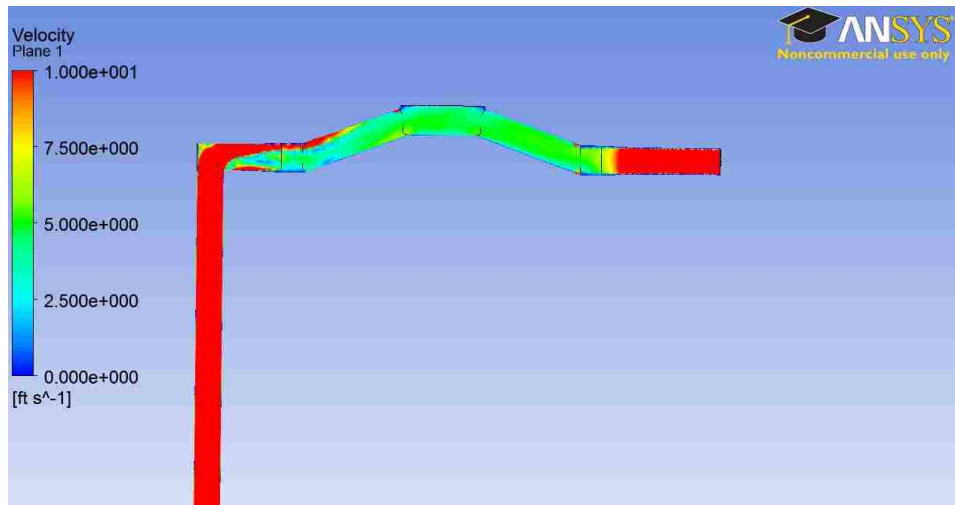


Figure 49: RT-4 velocity distribution through target cross-section using Fluent

Although not identical, the velocity streamlines and distribution shown in Figures 48 and 49 are comparable in overall shape to what is seen in CFX. This builds confidence that the models run in ANSYS CFX are accurate.

### 3.5.7. Experimental Verification

To further validate the ANSYS CFX model, a prototype of the RT-4 target was fabricated so a comparison of the experimental pressure drop across the target could be made to what was predicted in the ANSYS CFX model. 3D printing was used to fabricate the centermost piece of the target which includes the target chamber. The inlet and outlet chambers were constructed from aluminum and the three pieces were bolted together. Pressure taps were put along the inlet and outlet tubes.

Figure 50 shows the experimental setup for determining the pressure drop. Since the inlet feed is taken directly from the building water supply, a turbo pump was added to maintain a more constant flow rate. Two flow gauges and two differential pressure gauges were used in this experiment.

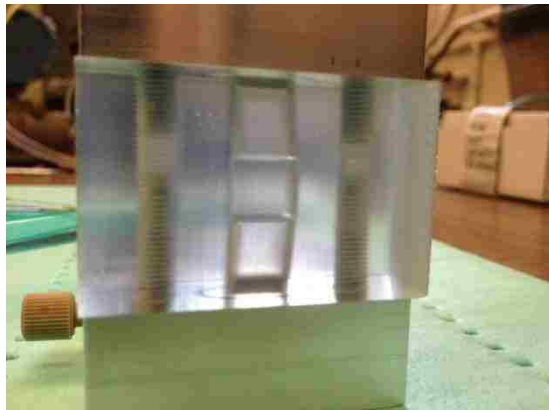
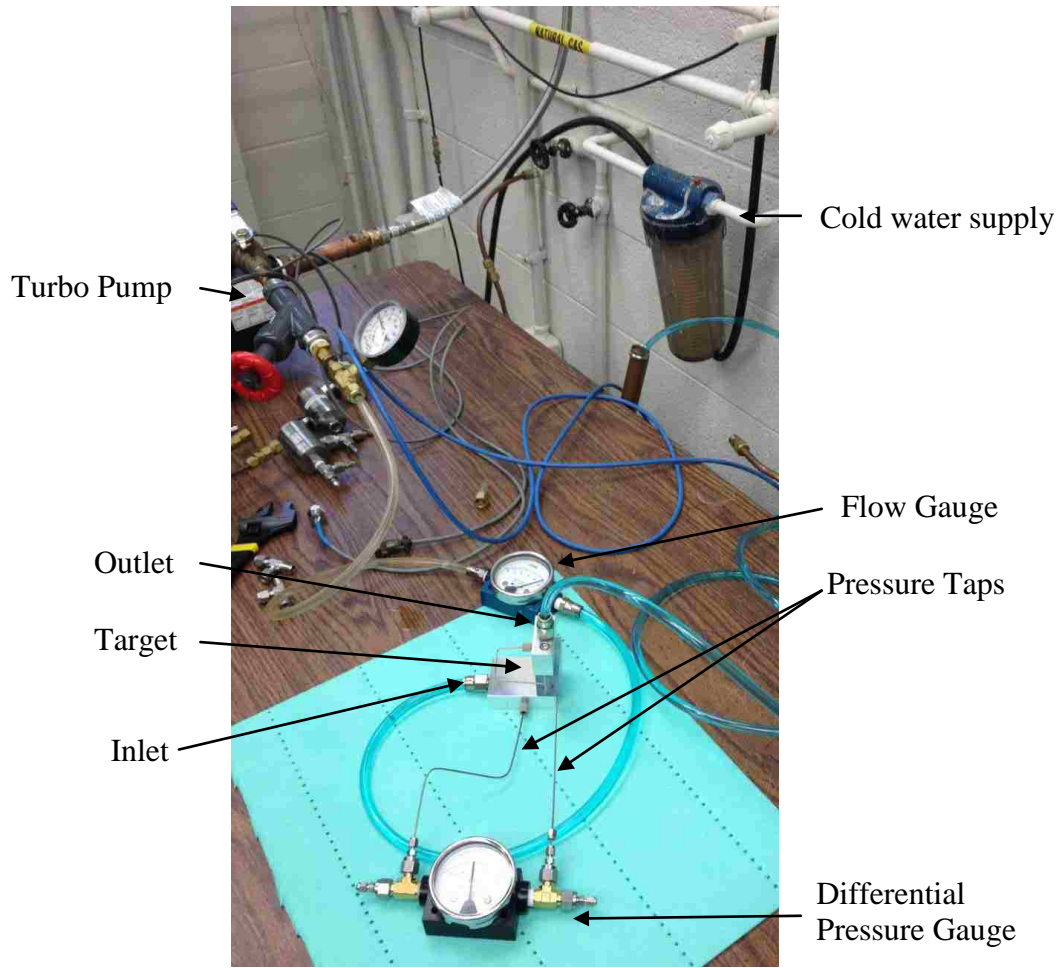


Figure 50: Pressure drop experimental setup (top) and close-up of printed target (bottom)

Figure 51 shows the experimentally measured pressure drop through the RT-4 printed target compared with that predicted in ANSYS CFX.

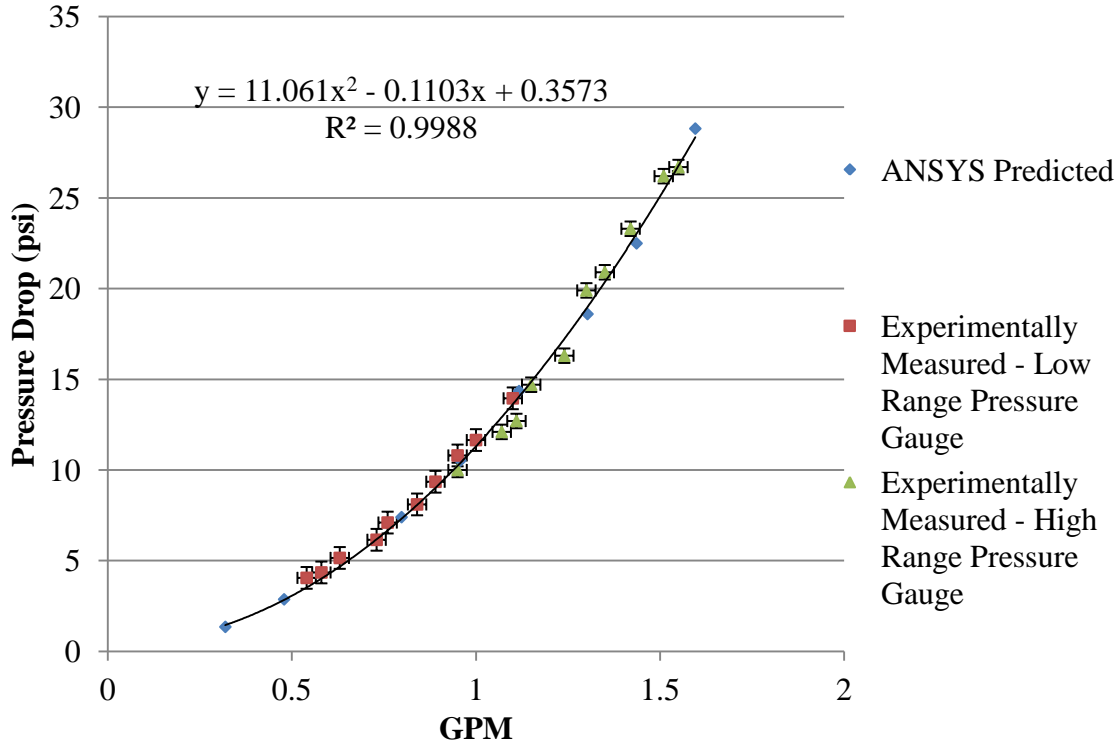


Figure 51: Experimental pressure drop vs. ANSYS predicted data

As shown, there is excellent agreement between the predicted pressure drop in CFX and the experimental pressure drop. Error bars were applied to data points based on the discretization of the gauges and the fluctuations seen in each measurement.

### 3.6. Target Comparison

The purpose of this section is to provide a complete overview of the evaluated target designs. The pressure drop, flow rate, system volume, and maximum temperatures are all shown in Table 9.

Table 9: Contending geometry design results

Target Type	System Pressure Drop (psi)	Flow Rate (GPM)	System Volume (ml)
RT-1	31.40	1.3727	14.47
RT-2	34.71	1.3392	8.85
RT-3	44.91	1.2357	9.87
RT-4	44.49	1.2400	8.04

Inlet Temp ( <sup>0</sup> F)	Heat Input (kW)	Maximum Temp ( <sup>0</sup> F)
101.65	2.70	258.0
102.89	2.70	451.3
104.59	2.70	196.0
104.54	2.70	238.8

### 3.7. Maximize Heat Input

By keeping the proton energy at 14 MeV and increasing the beam current, an estimate of when boiling will occur can be made as a function of the total heat input. Figure 52 shows the predicted maximum temperature at the window-fluid interface as a function of heat input. The maximum bulk temperature is also shown as a function of heat input. This becomes important if the restriction on allowing the window to surpass  $T_{sat}$  is relaxed. As mentioned in the Introduction, if the bulk fluid is still significantly subcooled when the window reaches the saturation temperature as is the case with the RT-4 target and the pump can handle up to 20% by volume vapor, it is possible that the limiting criteria is either the window reaching critical heat flux or the bulk fluid surpassing the saturation temperature. The following figure shows the maximum window-fluid interface and bulk fluid temperatures as a function of heat input.

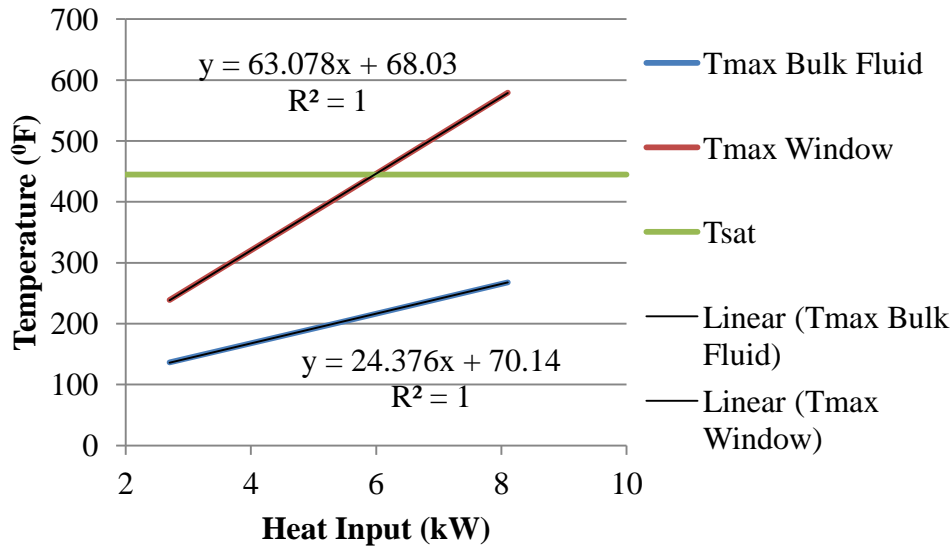


Figure 52: RT-4 temperature as a function of heat input

Using the linear projections of the maximum temperatures, the heat input which corresponds to the window and bulk fluid temperatures reaching saturation can be predicted. This is then correlated to the Curies of  $^{18}\text{F}$  produced to get a general idea of the capability of the RT-4 target.

Table 10: RT-4 maximum temperatures

RT-4, 14 MeV Protons				
<i>Limiting Condition</i>	<i>Heat Input (kW)</i>	<i>Beam (<math>\mu\text{A}</math>)</i>	<i>mCi/kW</i>	<i>Saturation Activity (Ci)</i>
Window reaches $T_{\text{sat}}$	5.97	426.42	16297.25	97.29
Bulk fluid reaches $T_{\text{sat}}$	15.36	1097.27	16297.25	250.36

### 3.7.1. Critical Heat Flux Estimation

Katto's generalized correlation for tubes was used to estimate the critical heat flux of the RT-4 target. For subcooled, high flow rate, high pressure, water systems the critical heat flux can be estimated using the following equations [21]:

$$\frac{q_{CHF,sat}}{Gh_{fg}} = 8.20 \left(\frac{\rho_v}{\rho_f}\right)^{0.65} \left(\frac{\sigma\rho_f}{G^2L}\right)^{0.453} \frac{1}{1+107\left(\frac{\left(\frac{\sigma\rho_f}{G^2L}\right)^{0.54} L}{d}\right)} \quad (43)$$

$$\left( \begin{array}{l} K_{HP}=0.664\left(\frac{\rho_v}{\rho_f}\right)^{-0.6} \text{ for } \frac{\sigma\rho_f}{G^2L}<4x10^{-8} \\ K_{HP}=3.08\left(\frac{\rho_v}{\rho_f}\right)^{-0.6} \left(\frac{\sigma\rho_f}{G^2L}\right)^{0.09} \text{ for } \frac{\sigma\rho_f}{G^2L}>4x10^{-8} \end{array} \right) \quad (44)$$

$$q_{CHF,sub} = q_{CHF,sat} \left(1 + K_{HP} \frac{\Delta h_{sub}}{h_{fg}}\right) \quad (45)$$

Using the total system flow rate of the RT-4 target and enthalpy of the fluid corresponding to the bulk fluid reaching the saturation temperature (15.36 kW), the critical heat flux was calculated to be 12,509 W/cm<sup>2</sup>, whereas the actual heat flux out of the window is 1,443 W/cm<sup>2</sup>. Therefore, although the correlation is not truly representative of target geometry, it does indicate that CHF is likely not reached by the time the bulk fluid reaches the saturation temperature. However, if additional heat is added such that the average outlet temperature of the target is at the saturation temperature, the CHF drops to 1,721 W/cm<sup>2</sup>. This indicates that CHF is likely not a concern at the beam currents being used in this study, however this may become a factor as more heat is applied.

Other correlations are available for geometries more representative of the target designs considered here, although each of these relations has its own disadvantages. Katto also developed a correlation for flow between parallel heated plates. However, this

correlation is for film flow of saturated water at a pressure of 14.7 psi and does not contain a subcooling term [21]. A subcooling term is necessary because at heat inputs corresponding to the window-fluid interface reaching the saturation temperature, the bulk fluid is still highly subcooled. This correlation is given as:

$$\frac{q_{CHF}}{Gh_{fg}} = 0.175 \left( \frac{\rho_g}{\rho_f} \right)^{0.467} \left( \frac{\sigma \rho_f}{G^2 L} \right)^{\frac{1}{3}} \left( 1 + \frac{\rho_g}{\rho_f} \right)^{1/3} \quad (46)$$

Using this relationship, the critical heat flux is estimated to be 1,224 W/cm<sup>2</sup>.

Similarly, Yagov developed a correlation comparable in structure to Katto's correlations for flow boiling over a disk heater mounted in a rectangular flow channel [21]. Geometrically, this is the most similar of the three correlations to the actual target design. However, this correlation is for saturated R12 refrigerant and is given as:

$$\frac{q_{CHF}}{Gh_{fg}} = 0.66 \left( \frac{\rho_g}{\rho_f} \right)^{0.604} \left( \frac{\sigma \rho_f}{G^2 L} \right)^{0.415} \quad (47)$$

Since this correlation has dimensionless groups, the fact that the coolant is intended for R12 may not be relevant as long as they span the same range as water. Lack of a subcooling component however, is more restrictive. Using this relationship, the critical heat flux is estimated to be 1,177 W/cm<sup>2</sup>. A copy of the code used to calculate these values is shown in Appendix E.



## Chapter 4 - Conclusions

Four target designs were evaluated for use in the integrated recirculating target system. Models of these target designs were analyzed using the Computational Fluid Dynamics program ANSYS CFX. These models have provided valuable information as to the temperature and flow distributions expected inside the target models.

The Recirculating Target 4 (RT-4) design was selected for its superior combination of efficient heat transfer, simplistic design, and fabricability. In addition to the models produced in ANSYS CFX, RT-4 was further validated by a secondary analysis of the flow distribution in Fluent, as well as experimental verification of the pressure drop using a prototype printed target.

From the models produced in ANSYS CFX, this target is projected to be capable of taking 6 kW of heat input before the window reaches the saturation temperature, for a total production of 97.29 Ci of  $^{18}\text{F}$ . If subcooled boiling at the window is allowed, over 15 kW of heat can be accommodated before any part of the bulk fluid reaches the saturation temperature, resulting in 250.36 Ci of  $^{18}\text{F}$  being produced.

## 4.1 Future Work

RT-4 will need to be experimentally tested in order to determine the true capabilities of the system as ANSYS CFX is not capable of modeling boiling inside the target. The system can be limited by any of the following:

- Local subcooled boiling at the window
- Critical heat flux at the window
- Vapor lock in the pump from too high of a vapor fraction
- Excess void fraction from bulk fluid boiling, causing the beam to hit the back of the target

Although correlations exist to determine the critical heat flux in flow boiling systems, it is not clear that these correlations can be applied to the recirculating target system with confidence given the nature of cyclotron proton beam heating. However, from best estimates it can be concluded that given the recommended heat inputs, CHF is likely not a concern. Still, critical heat flux experiments under operating conditions representative of the recirculating target system should be conducted if beam currents are to be increased further.

Also, in order to verify the velocity distributions predicted by the CFX model, a particle-track experiment can be done. The printed version of the RT-4 target is transparent and Bruce Technologies Inc. has access to a high speed camera. Diamond nanoparticles illuminated by UV light could be used to visualize the streamlines through the target.

As a longer-term project, an area for research is using a nanofluid (colloidal suspension of nanoparticles in a fluid) such as diamond nanoparticles suspended in target

water to enhance the heat transfer characteristics of the target fluid. It was found that the nanoparticles increase the wettability of the surface and these high conductivity particles significantly increase the bulk thermal conductivity of the fluid [14]. Since the recirculating target system is limited by boiling, this may be an opportunity to further improve the capacity of both the recirculating target system as well as batch style targets. A study found that nanofluids can increase CHF in pool boiling systems by as much as 200% and flow boiling systems between 40-50% [14]. The most significant challenge for utilizing diamond nanoparticles will be their extraction from the colloidal suspension.

## Bibliography

- [1] Clark, John C. *High-Powered Cyclotron Recirculating Targets for Production of the  $^{18}\text{F}$  Radionuclide*. Master's Thesis. Department of Nuclear Engineering North Carolina State University, December 2004.
- [2] Newnam R.P. *High Capacity Heat Exchangers for Recirculating  $^{18}\text{F}$  Radionuclide Production Targets*. Master's Thesis. Department of Nuclear Engineering, North Carolina State University, May 2007.
- [3] *ANSYS CFX Introduction*. 2010. ANSYS CFX 13.0 Manual.
- [4] *ANSYS CFX-Solver Modeling Guide*. 2009. ANSYS CFX 12.0 Manual.
- [5] Blokland, J., P. Trindev, M. Stokkel, and E. Pauwels. "Positron Emission Tomography: A Technical Introduction from Clinicians." *European Journal of Radiology* 44(2002): 70-75. Web.
- [6] Shaeffer, M. C., F. Barreto, J. R. Datesh, and B. R. Goldstein. *Design of a  $^{18}\text{F}$  Production System at ORNL 86-Inch Cyclotron*. Tech. Oak Ridge National Laboratory, 1977.
- [7] Chu, Y. E., S. D. Engstrom, and D. G. Sundberg. *Design of a Fluorine-18 Production System at ORNL Cyclotron Facility, Part 2*. Tech. Oak Ridge National Laboratory, 1977.
- [8] *Iba RadioPharma Solutions*. Brussels, France. Web. <<http://www.iba-worldwide.com/gateway>>
- [9] Kiselev, M. Y., and Duc Lai. Process and Apparatus for Production of F-18 Fluoride. Patent 6,567,492 B2. 20 May 2003. Print.
- [10] *ST21 Series DC Brushless Regenerative Turbine Pumps*. MTH Pumps. Web. <<http://www.mthpumps.com/english/st21.html>>
- [11] *Solidworks*. Dassault Systemes. Web. <<http://www.solidworks.com>>
- [12] *Miniature Heat Exchangers*. Exergy, LLC, 27 May 2008. Web. <<http://exergyllc.com/>>.
- [13] Pelowitz, D. B. *MCNPX<sup>TM</sup> USER'S MANUAL*. Apr. 2011. Version 2.7.0..

- [14] Kim, S. J. *Subcooled Flow Boiling Heat Transfer and Critical Heat Flux in Water-Based Nanofluids at Low Pressure*. Diss. Massachusetts Institute of Technology. Department of Nuclear Science and Engineering, 2009.
- [15] Stokely, M. H. *Advanced Thermosyphone Targets for Production of the  $^{18}\text{F}$  Radionuclide*. Master's Thesis. Department of Nuclear Engineering, North Carolina State University, March 2007.
- [16] *Meshing Help*. 2009. ANSYS CFX 12.0 Manual.
- [17] Wilkes, J. O. *Fluid Mechanics for Chemical Engineers*. 2<sup>nd</sup> ed. Prentice Hall, 2008.
- [18] *ANSYS CFX-Solver Theory Guide*. ANSYS CFX 12.0 Manual.
- [19] Idelchik, I. E. *Handbook of Hydraulic Resistance*. Third Edition: CRC, 1994.
- [20] Incropera, Frank P., David P. Dewitt, Theodore L. Bergman, and Adrienne S. Lavine. *Fundamentals of Heat and Mass Transfer*. 6th ed. John Wiley & Sons, 2007.
- [21] Kang, Y. T. *Experimental Investigation of Critical Heat Flux in Transient Boiling Systems with Vertical Thin Rectangular Parallel Plate Channels*. Diss. Ohio State University. Department of Mechanical Engineering, 1994.
- [22] Stokely, Matt H. *Calculation*. Jan. 2013. Independent analysis of proton beam
- [23] Lamarsh, John R., and Anthony J. Baratta. *Introduction to Nuclear Engineering*. 3rd ed. Upper Saddle River: Prentice Hall, 2001.
- [24] Stokely, Matt H. "Pump Pressure Curves." 2 July 2012. E-mail.
- [25] Jones, W. P., and B. E. Launder. "The Prediction of Laminarization with a Two-Equation Model of Turbulence." *International Journal of Heat and Mass Transfer* 15 (1972): 301-14.
- [26] Menter, F. R. "Two-equation Eddy-viscosity Turbulence Models for Engineering Applications." *AIAA Journal* 32 (1994): 269-89.
- [27] Wieland, Bruce W., and Bruce C. Wright. Recirculating Target and Method for Producing Radionuclide. Duke University, assignee. Patent EP1575488 B1. 20 May 2003.

# Appendices

# Appendix A

## Sample System Volumetric Flow Rate MATLAB Code

```
%Calculating system mass flow rate
function F=flow(X)

x=X(1)

%Component pressure drop equations
target = 57.132.*x.^2+1.3491.*x + 0.017      %RT-1 dP Curve
HE1 = 4.4379.*x.^2-0.7200.*x+1.374
HE2 = 4.0963*x^2+1.398*x-0.7037
elbow = 2.31.*x
pump = -98.606.*x+166.76

%Piping
rho = 61.73;                                %lbm/ft3
mu = 3.7583E-4;                             %lbm/s/F
D = 0.0104;                                  %1/8 in. tubing
v = x*26.197;                                %constant to get ft/s from gpm
L = 0.5;                                      %ft (guessed amount of piping)

%Constants
Re = rho*v*D/mu;
f = 0.184*Re^-0.2;                           %friction factor
dp = (f*L/D)*(rho*v^2/2);
piping = dp*(2.158E-4);                      %Convert lbm/ft/s2 to psi

%Final eqn
F(1) = pump-target-HE1-HE2-elbow-piping;

end
```

## Sample System Stream Temperatures MATLAB Code

```
%Calculating temperatures through the integrated system
```

```
function F=temp(X)
```

```
%Variables
```

```
T1 = X(1);  
T2 = X(2);  
T3 = X(3);  
Tc1 = X(4);  
Tc2 = X(5);
```

```
%Constants
```

```
VolumetricFR = 1.3727;           %gpm  
mdot = 495.20*VolumetricFR;      %lbm/hr  
mc = 1499.2;                      %lbm/hr; 3 gpm  
cp = 0.997;                       %Btu/lbm/F
```

```
%Calculate UA1 & UA2
```

```
UA1 = 86.41  
UA2 = 175.61
```

```
%Equations
```

```
Q2 = UA1*((T3-60)-(T2-Tc1))/log((T3-60)/(T2-Tc1));  
Q3 = UA2*((T1-60)-(T3-Tc2))/log((T1-60)/(T3-Tc2));  
Qc1 = mc*cp*(Tc1-60);  
Qc2 = mc*cp*(Tc2-60);  
F(1) = mdot*cp*(T2-T1)-9212.78;      %2.7kW as BTU/hr  
F(2) = mdot*cp*(T2-T3)-Q2;  
F(3) = mdot*cp*(T2-T3)-Qc1;  
F(4) = mdot*cp*(T3-T1)-Qc2;  
F(5) = mdot*cp*(T3-T1)-Q3;
```

```
MATD = (T2+T3)/2-(Tc1+60)/2
```

```
end
```



# Sample Exergy Heat Exchanger Calculator Output Data

Model Number: 00268-01 (10 Series HX, 8 Inch Tube Bundle)

Tube Side (product): Water

Shell Side (working): Water

Flow Rate: 1.240 gal/min

Flow Rate: 3 gal/min

Inlet Temperature: 98.69 F

Inlet Temperature: 60 F

Inlet Pressure: 400 psig

Inlet Pressure: 1 atm

Submit

English Units		
Heat Exchanger Model	00268-01	
	Tube Side	Shell Side
Fluid	Water	Water
Temperature In	98.69	60 F
Temperature Out	89.57	63.74 F
Mass Flow	615.83	1498.34 lb/hr
Volumetric Flow	1.24	3 gpm
Pressure Drop	5.11	100.63 psi
Heat Transfer	5606	BTU/hr
Effectiveness	0.236	

Metric Units		
Heat Exchanger Model	00268-01	
	Tube Side	Shell Side
Fluid	Water	Water
Temperature In	37.05	15.56 C
Temperature Out	31.98	17.63 C
Mass Flow	77.59	188.79 g/sec
Volumetric Flow	4.69	11.36 lpm
Pressure Drop	35.23	693.82 kPa
Heat Transfer	1642	Watts
Effectiveness	0.236	

# Appendix B

## Gaussian Standard Deviation and Plot Code

```
%Calculate S.D. necessary to reach 85%
Select = 0.85;

%Initial Conditions
Error = 1.0;
sigmax = 2;
sigmay = sigmax;

%Solve for S.D.
while Error>0.001
diameter = 10;
radius = diameter/2;
F = @(r,t) r.*1/(2.*pi.*sigmax.*sigmay).*exp(-
r.^2.*cos(t).^2/(2.*sigmax.^2)).*exp(-r.^2.*sin(t).^2/(2.*sigmay.^2));
I = quad2d(F,0,radius,0,2.*pi)

Error = abs((Select-I)/Select);
sigmax = sigmax+0.001;
sigmay=sigmax;
end

%Input
x=[-10:0.5:10];
y=[-10:0.5:10];

%Gaussian
[x,y] = meshgrid(x,y);
z=normpdf(x,0,sigmax).*normpdf(y,0,sigmax);

%plotting
subplot(2,2,2)
surf(x,y,z)
subplot(2,2,1)
pcolor(x,y,z)
```

# Appendix C

## Sample MCNPX Input Deck

```
14 Mev Protons in Water
c Mesh Energy Deposition
c
c
c --- cell cards ---
c
c HAVAR
  1 1 -8.3 -1 2 -3 imp:h=1
c WATER
  2 2 -1 -1 3 -4 imp:h=1
c OUTSIDE UNIVERSE
  3 0 1:-2:4 imp:h=0

c --- surface cards ---
c
  1 cz 0.5
  2 pz 0
  3 pz 0.00254
  4 pz 1.5

c --- material cards ---
c
c Material #1: Havar
m1 27000 -0.42 26000 -0.195 24000 -0.191 28000 -0.127 &
    74000 -0.027 42000 -0.022 25000 -0.016 6000 -0.002
c Material #2: H2O
m2 HLIB=24h 1001.24h -0.1119 8016.24h -0.8881
c --- data cards ---
mode h
phys:h 14.0 j 0. j
cut:h 0.05
c mode is set to protons with the energy range 14 Mev max and 50 kev min
lca j j j
nps 20000
F1:H 2
c the next 7 lines are the energy deposition mesh
TMESH
CMESH3 total
ERESH3 0.0 14.0
  CORA3 0.0 .02381 17i .47619 0.50
  CORB3 0.0 0.00254 0.023684211204 17i 0.876315788796 0.9
  CORC3 360
ENDMD
c
c --- source definition ---
c 27 MeV Proton Beam
SDEF SUR=2 DIR=1 vec=0. 0. 1. erg=14. PAR=h pos=0. 0. 0. x=d5 y=d3 z=0 CCC=1
SC3 85% Gaussian Distribution at 5.0mm
SP3 -41 0.604 0
SC5 85% Gaussian Distribution at 5.0mm
SP5 -41 0.604 0
```



# Appendix D

## Sample Convergence Plots

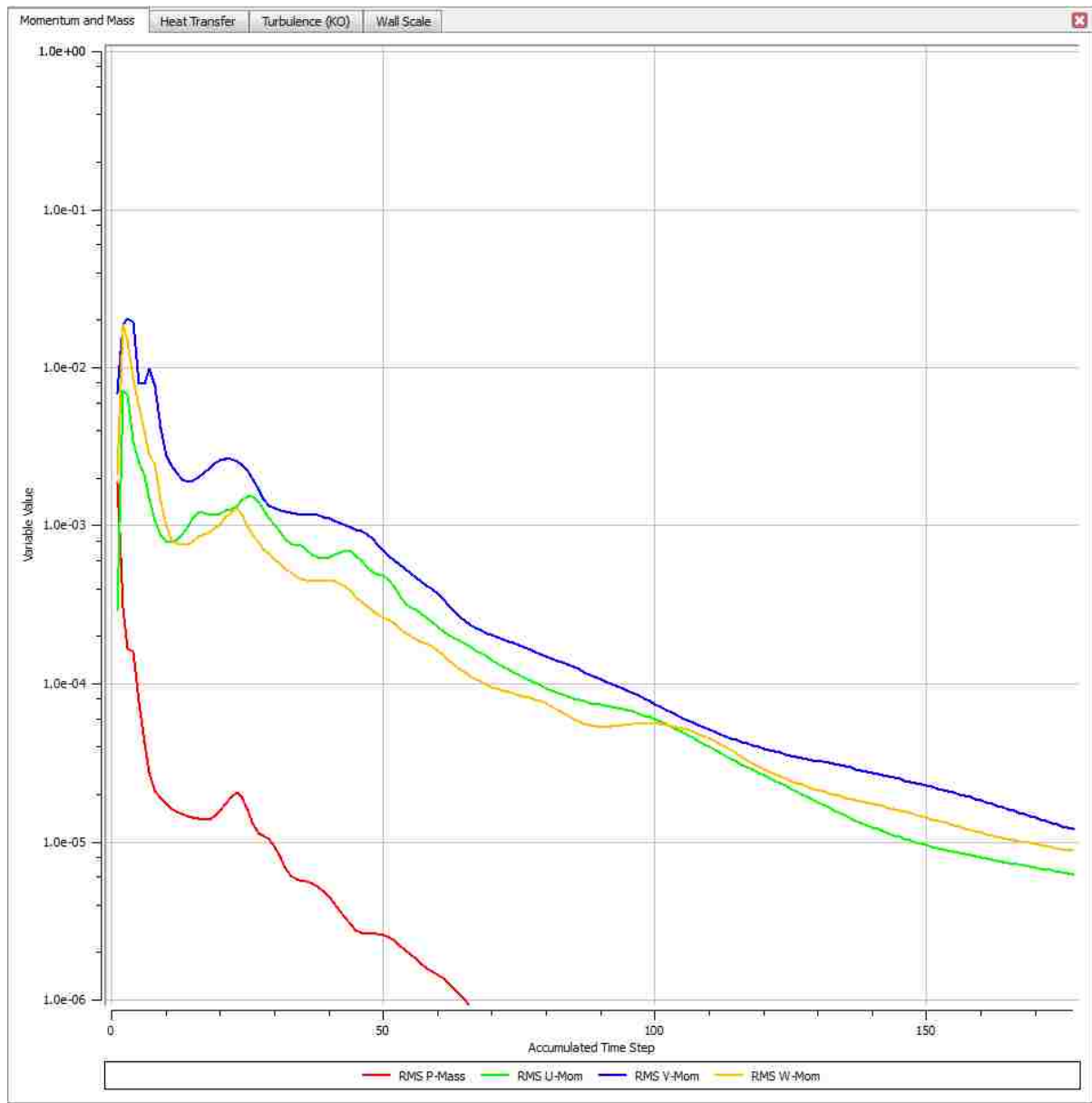


Figure D 1: Mass and momentum residuals plot for RT-4

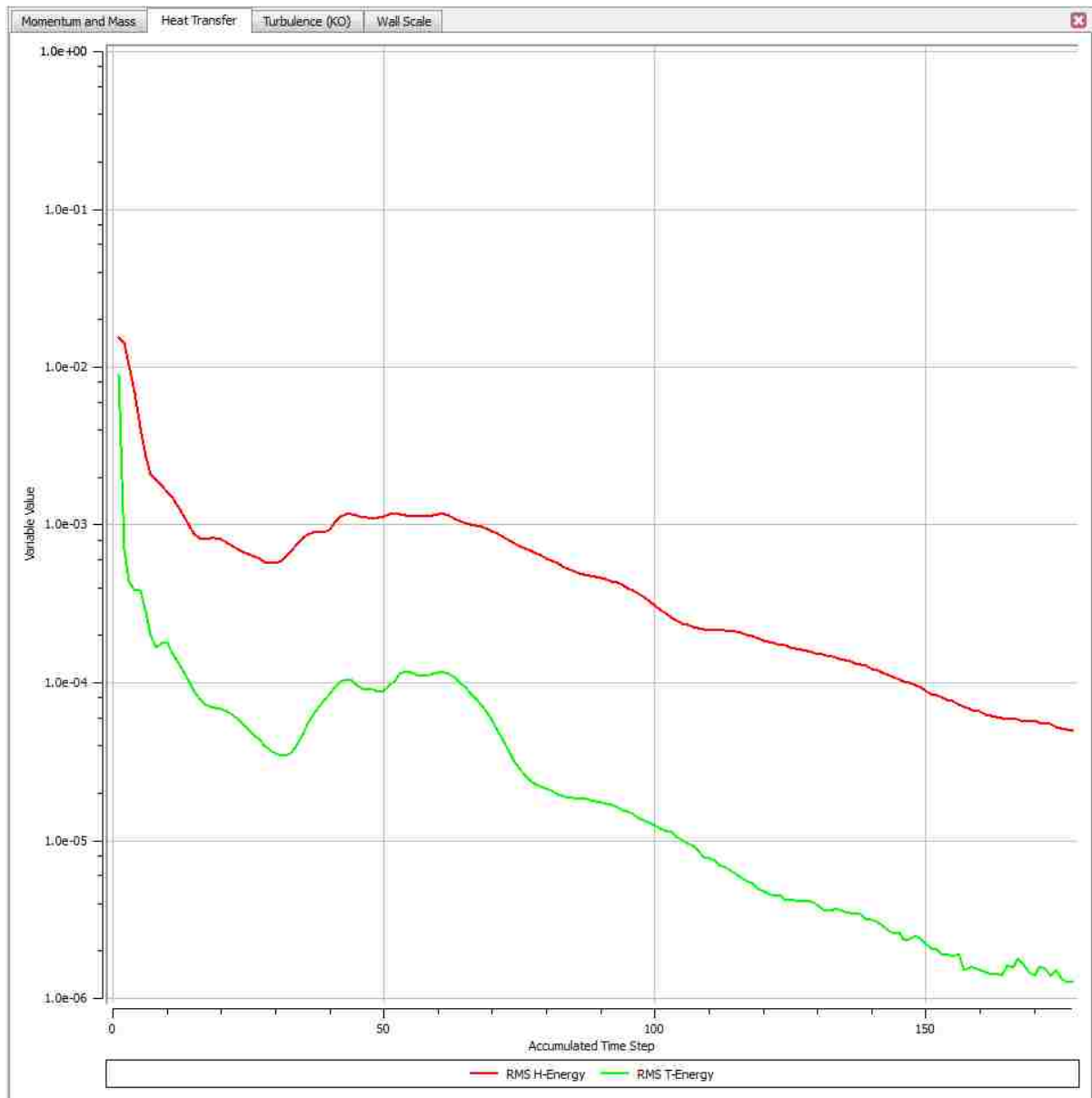


Figure D 2: Heat transfer residuals plot for RT-4

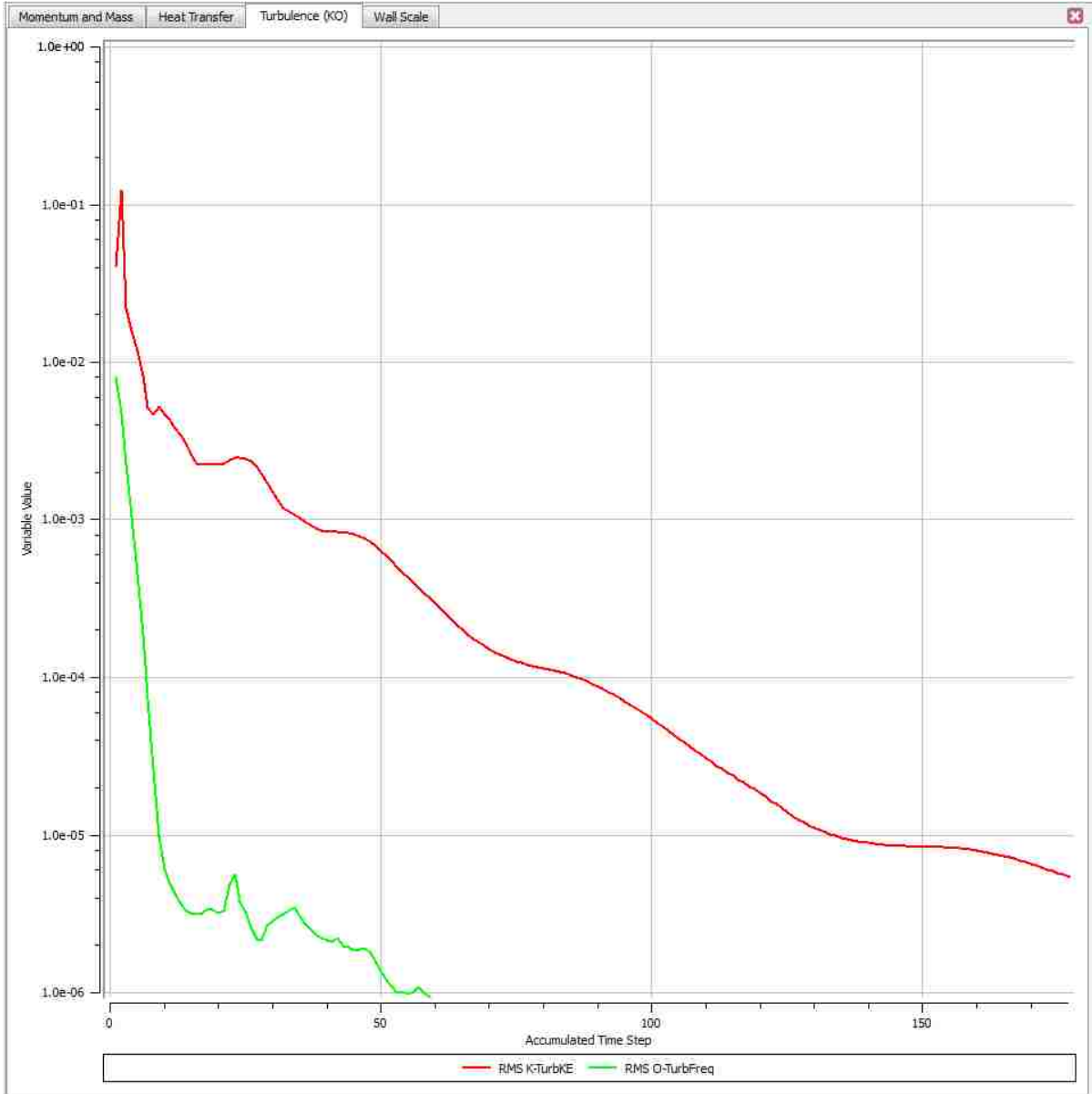


Figure D 3: Turbulence residuals plot for RT-4

# Appendix E

## Critical Heat Flux Calculation Code

```
%Critical heat flux calculation

mdot = 0.1713 ;           %[lb/s]
Ax = 0.000366127;       %[ft^2]
G = mdot/Ax ;           %[lbm/ft2/s]
hfg = 780.4;           %[BTU/lb]
rhog = 0.861;           %[lbm/ft3]
rhol = 51.706;
sigma = 2.56E-3;        %[lb/ft]
L = 0.0328;            %[ft] --> 10mm beam
d = 0.01476;          %[ft] --> 4.5mm deep
h = 158.73;
hf = 424.2;

%Flow through a tube
qTi =
G*hfg*8.20*(rhog/rhol)^0.65*(sigma*rhol/G^2/L*32.2)^0.453*(1/(1+107*((sigma
a*rhol/G^2/L*32.2)^0.54*L/d)));

qT = qTi*3600*3.5125/(100^2)    %BTU/s/ft2 to W/cm2

if (sigma*rhol/G^2/L*32.2) < 4E-8;
    K = 0.664*(rhog/rhol)^-0.6;
else
    K = 3.08*(rhog/rhol)^-0.6*(sigma*rhol/G^2/L*32.2)^0.09;
end

qTsub = qT*(1+K*(hf-h)/hfg)

%Flow over a disk heater
qDi = G*hfg*0.66*(rhog/rhol)^0.604*(sigma*rhol/G^2/L*32.2)^0.415;
qD = qDi*3600*3.5125/(100^2)

%Flow through parallel plates
qPi = G*hfg*0.186*(rhog/rhol)^0.559*(sigma*rhol/G^2/L*32.2)^0.264;
qP = qPi*3600*3.5125/(100^2)
```